Holographic Localization With Synthetic Reconfigurable Intelligent Surfaces

Ziyi Wang , *Graduate Student Member, IEEE*, Zhenyu Liu , *Member, IEEE*, Yuan Shen , *Senior Member, IEEE*, Andrea Conti , *Fellow, IEEE*, and Moe Z. Win , *Fellow, IEEE*

Abstract—**Reconfigurable intelligent surfaces (RISs) are proposed to control complex wireless environments in next-generation networks. In particular, wideband RISs can play a key role in high-accuracy location awareness, which calls for models that consider the frequency-selectivity of metasurfaces. This paper presents a general signal model for wideband systems with RISs and establishes a Fisher information analysis to determine the theoretical limits of wideband localization with RISs. In addition, synthetic RISs are proposed to mitigate the multiplicative fading effect caused by the scattering property of RISs. Special scenarios including complete coupling and complete decoupling are further investigated. Results show that with the proposed models, a wideband RIS with a polynomial phase response per element provides more position information than those with more degrees of freedom (DOFs) in piecewise-constant phase response per element. Furthermore, velocity-induced information allows a dynamic RIS to provide more position information than a static RIS. Additionally, a dynamic RIS can be synthesized through multiple measurements to outperform a large one.**

Index Terms—**Fisher information, localization, near-field propagation, next-generation networks, reconfigurable intelligent surfaces, wideband system.**

I. INTRODUCTION

HOLOGRAPHIC LOCALIZATION, empowered by reconfigurable intelligent surfaces (RISs) to achieve controllable electromagnetic (EM) environments, is promising in next-generation wireless systems [1]. Its applications include smart environments [2], [3], integrated sensing and communication (ISAC) [4], [5], [6], [7], distributed networks [8], [9], [10], [11], [12], and Internet-of-Things (IoT) [13], [14], [15], [16]. However, the potential of holographic radio has been limited by the frequency-selectivity [17], [18], [19], [20] and the multiplicative fading effect [21] of RISs. In particular, holographic localization approaches so far are constrained with a narrowband or constant-phase-response assumption on RISs. Moreover, existing approaches mitigate the multiplicative fading effect by setting a large-aperture RISs [22], [23] or integrating power amplifiers (PAs) to RIS elements [21]. Nevertheless, the mitigation of the multiplicative fading effect may introduce additional hardware costs and power consumption as well as reduce the system robustness [22], [24]. Similar issues also exist in RIS-aided near-field communication and sensing, which has piqued significant research interest recently [25], [26], [27], [28].

RISs can be used to improve the accuracy of localization systems due to their reconfigurability and low power consumption [29], [30], [31]. Nevertheless, most existing works related to localization with RISs are based on a narrowband assumption [32], [33], [34], [35]. With such an assumption, RISs can be simplified as devices that control the additional phase shift of each element for the reflected EM waves. Even though some works consider wideband transmitted signals, they assume that the phase responses of RIS elements are constant over the considered frequency band [36], [37], [38], [39]. Other works related to wideband localization with RISs partitioned the frequency band into multiple narrow frequency bands [40], but they still assume that the phase responses of RIS elements are the same in each narrow band. Also, such frequency band partitions demand high degrees of freedom (DOFs) for every RIS element configuration and may increase the fabrication complexity. This assumption is unnecessary and limits the potential of RISs. In fact, it has been shown that phase response over a frequency band can be designed to be non-constant [41], [42].

Aside from the operational frequency band, another limitation for wireless systems with RISs is the multiplicative fading effect due to the scattering property of RISs. With the fading effect, the strength of signal components scattered by the RISs can be weakened, thus attenuating the benefits from the controllable environments. To address this issue, a new RIS architecture, active RISs, is proposed with integrated PAs on all RIS elements [21]. However, the additional PAs can increase power consumption and fabrication costs. Furthermore, additional configurations [43] are required to avoid significantly amplifying the mutual coupling between RIS elements and the multiple reflections between the RIS elements and environments. In

Ziyi Wang is with the Department of Information Technology and Electrical Engineering, ETH Zurich, 8092 Zurich, Switzerland (e-mail: ziywang@student.ethz.ch).

Zhenyu Liu is with the Tsinghua Shenzhen International Graduate School, Tsinghua University, Shenzhen 518055, China (e-mail: zhenyuliu@sz.tsinghua.edu.cn).

Yuan Shen is with the Department of Electronic Engineering, Tsinghua University, Beijing 100084, China (e-mail: shenyuan_ee@tsinghua.edu.cn).

Andrea Conti is with the Department of Engineering and CNIT, University of Ferrara, 44122 Ferrara, Italy (e-mail: a.conti@ieee.org).

Moe Z. Win is with the Laboratory for Information and Decision Systems, Massachusetts Institute of Technology, Cambridge, MA 02139 USA (e-mail: moewin@mit.edu).

Digital Object Identifier 10.1109/JSTSP.2024.3435465

fact, the multiplicative fading effect can also be mitigated by synthetic RISs without any hardware modifications and without amplification of interference. This paper introduces the concept of synthetic RISs, which are virtual dynamic RISs synthesized from the dynamic RISs over different observation intervals.

The fundamental questions related to wideband holographic localization with RISs are: (i) what is the wideband model for the received signal in the presence of RISs; (ii) how do RISs improve localization in wideband systems; and (iii) to what extent can synthetic RISs mitigate the multiplicative fading effect? Answers to these questions provide insights into the design and analysis of wideband holographic localization systems with synthetic RISs. The goal of this paper is to determine the fundamental limits of holograpic localization with wideband RISs in both near- and far-field scenarios and to quantify the performance gain introduced by the motion of dynamic RISs and synthetic RISs. In this paper, the narrowband assumption on RISs is removed and the dynamic wideband RISs are synthesized to mitigate the multiplicative fading effect. The key idea is to characterize the phase responses of RIS elements with finite polynomial coefficients and to exploit the velocity-induced position information with the temporal cooperation among dynamic RISs in different positions to significantly enhance the information brought by RISs.

This paper presents general signal models for wireless environments with wideband RISs and establishes the performance limits of RIS-aided wideband localization. The key contributions of this paper include:

- modeling of near/far-field[1] signals for wireless environments with wideband RISs, where the spherical wavefront, polarization attenuation, and polynomial phase response are considered under the angular insensitivity assumption on RIS elements;
- derivation of theoretical limits for wideband localization via static RISs, dynamic RISs, and synthetic RISs including scenarios with the complete coupling (CC) and complete decoupling (CD) of the signal components scattered by different RIS elements;
- analysis of the difference in the position information provided by dynamic RISs and synthetic RISs, revealing the essential distinction between large-aperture and synthetic-aperture RISs; and
- quantification of the localization performance in CC and CD scenarios, highlighting the importance of the proposed wideband model and evaluating the role of both velocity-induced information and RIS trajectory for constructing a synthetic RIS.

The remaining sections of this paper are organized as follows. Section II presents near/far-field signal models for holographic localization with static RISs and with dynamic RISs. Section III performs Fisher information analysis for holographic localization with static RISs, dynamic RISs, and synthetic RISs. Section IV presents a case study for holographic localization with numerical results. Section V presents our conclusion.

---

[1]The near-field regime in this paper refers to the radiative near-field regime, which is considered in most existing works of wireless communications. The far-field model is a special case of the proposed near-field model, and thus the proposed models are applicable in both near- and far-field scenarios.

Notations: Random variables are displayed in sans serif, upright fonts; their realizations in serif, italic fonts. Vectors and matrices are denoted by bold lowercase and uppercase letters, respectively. Sets and collections are denoted by calligraphic font. Notation $\boldsymbol{A} \succcurlyeq \boldsymbol{B}$ denotes that $\boldsymbol{A} - \boldsymbol{B}$ is positive semi-definite. Define $\kappa(\boldsymbol{X}) = \boldsymbol{X} + \boldsymbol{X}^{\mathrm{T}}$, where $\boldsymbol{X}$ is a square matrix and $\boldsymbol{X}^{\mathrm{T}}$ is its transpose. The notations $[\boldsymbol{X}]_{i,j}$ and $[\boldsymbol{X}]_{i:j,k:l}$ respectively refer to the (i,j)-th element and the submatrix composed of rows i to j and columns k to l of the matrix $\boldsymbol{X}$. The m-by-n matrix of zeros (resp. ones) is denoted by $\boldsymbol{0}_{m \times n}$ (resp. $\boldsymbol{1}_{m \times n}$); when $n = 1$, the m-dimensional vector of zeros (resp. ones) is simply denoted by $\boldsymbol{0}_m$ (resp. $\boldsymbol{1}_m$). The symbol diag$\{\boldsymbol{X}_1, \boldsymbol{X}_2, \dots, \boldsymbol{X}_n\}$ denotes a block-diagonal matrix with diagonal blocks $\boldsymbol{X}_1, \boldsymbol{X}_2, \dots, \boldsymbol{X}_n$. The operator $|\cdot|$ takes the modulus of complex numbers, $\|\cdot\|$ takes the ℓ_2 norm of vectors, and $\langle \boldsymbol{x}, \boldsymbol{y} \rangle$ takes the inner product of vectors $\boldsymbol{x}$ and $\boldsymbol{y}$. The symbol $\jmath$ denotes the imaginary unit. The operator $\mathscr{F}\{\cdot\}$ generates the Fourier transform of its argument. The operators $\odot$ and $\otimes$ denote the Hadamard product and cross product, respectively. The ket $|\boldsymbol{p}_{\mathrm{t}} \rightarrow \boldsymbol{p}_{\mathrm{r}}\rangle$ denotes the polarization state of the EM wave traveling from position $\boldsymbol{p}_{\mathrm{t}}$ to position $\boldsymbol{p}_{\mathrm{r}}$. In this context, the polarization state can be viewed as a vector in $\mathbb{C}^3$, and the bra $\langle \boldsymbol{p}_{\mathrm{t}} \rightarrow \boldsymbol{p}_{\mathrm{r}}|$ can be viewed as the conjugate transpose of the vector. Define the direction vector $\boldsymbol{q}_0(\psi, \varphi) = [\sin(\psi)\cos(\varphi) \quad \sin(\psi)\sin(\varphi) \quad \cos(\psi)]^{\mathrm{T}}$, where $\psi \in [0, \pi]$, $\varphi \in [0, 2\pi)$. Moreover, define $(\psi_{\mathrm{A}}, \varphi_{\mathrm{A}}) = ((\pi - \psi) \bmod \pi, (\pi + \varphi) \bmod 2\pi)$. The symbols used for important quantities are summarized in Table I.

II. SYSTEM MODEL

This section proposes two signal models for the localization system: one with a static wideband RIS and another with a dynamic wideband RIS. Each model is applicable to both near- and far-field scenarios. In these models, the wideband RIS is defined as an RIS whose phase response at each element can be controlled independently.

A. Wideband Signal Model for Static RISs

Consider a three-dimensional (3D) scenario with one wideband N_{s}-element RIS, one agent that acts as a receiver (Rx), and N_{b} anchors that act as transmitters (Txs), as shown in Fig. 1. The agent is a node with an unknown position, and the anchors are nodes with known positions. Denote the coordinates of the m-th element on the wideband RIS, the agent, and the j-th anchor respectively by $\boldsymbol{p}^{(m)}, \boldsymbol{p}, \boldsymbol{p}_j \in \mathbb{R}^3$. The sets of anchors and RIS elements are denoted by $\mathcal{N}_{\mathrm{b}} = \{1, 2, \dots, N_{\mathrm{b}}\}$ and $\mathcal{N}_{\mathrm{s}} = \{1, 2, \dots, N_{\mathrm{s}}\}$, respectively. The objective of the system is to localize the agent using the received signal at the agent. Here, the agent at $\boldsymbol{p}$ and the anchors at $\boldsymbol{p}_j$, $j \in \mathcal{N}_{\mathrm{b}}$, could be placed in either the near- or far-field regimes of the RIS. We consider that the dimension of the RIS is much larger than the center wavelength λ_{c} to ensure diffraction effects insignificant.

The received signal at the agent from the the j-th anchor is

$$\mathsf{r}_j(t) = \chi_j r_j^{\mathrm{DP}}(t) + \sum_{m \in \mathcal{N}_{\mathrm{s}}} r_j^{\mathrm{RIS}(m)}(t) + \mathsf{z}_j(t) \qquad (1)$$

TABLE I
NOTATIONS OF IMPORTANT QUANTITIES

Notation	Definition	Notation	Definition
f_c	Center frequency of the transmitted signal	λ_c	Wavelength corresponding to the center frequency of the transmitted signal
$\boldsymbol{p}$	Position of the agent	N_0	One-sided PSD of white Gaussian noise
$\boldsymbol{p}_j$	Position of the j-th anchor	$\boldsymbol{p}^{(m)}$	Position of the m-th RIS element
$A_j^{\mathrm{DP}}(f)$	Aperture of the Rx antenna at the agent along the direction of the direct path from the j-th anchor	$A^{\mathrm{RIS}(m)}(f)$	Aperture of the Rx antenna at the agent along the direction of the scattering path via the m-th RIS element
$G_j^{\mathrm{DP}}(f)$	Gain of the Tx antenna at the j-th anchor along the direction of the direct path to the agent	$G_j^{\mathrm{RIS}(m)}(f)$	Gain of the Tx antenna at the j-th anchor along the direction of the scattering path via the m-th element
$D^{\mathrm{Rx}}(\psi, \varphi)$	Directivity function of the Rx antenna at the agent	$D_j^{\mathrm{Tx}}(\psi, \varphi)$	Directivity function of the Tx antenna at the j-th anchor
γ_j^{DP}	Polarization coefficient of the direct path between the agent and the j-th anchor	$\gamma_j^{\mathrm{RIS}(m)}$	Polarization coefficient of the scattering path starting at the j-th anchor via the m-th RIS element
α_j^{DP}	Attenuation of the direct path from the j-th anchor to the agent	τ_j^{DP}	Delay of the direct path from the j-th anchor to the agent
$\alpha_j^{\mathrm{IP}(m)}$	Attenuation of the incidence path from the j-th anchor to the m-th RIS element	$\tau_j^{\mathrm{IP}(m)}$	Delay of the incidence path from the j-th anchor to the m-th RIS element
$\alpha^{\mathrm{SP}(m)}$	Attenuation of the reflection path from the m-th RIS element to the agent	$\tau^{\mathrm{SP}(m)}$	Delay of the reflection path from the m-th RIS element to the agent
$\hat{\nu}_j^{\mathrm{IP}(m)}$	Normalized speed of the m-th RIS element relative to the j-th anchor	$\hat{\nu}^{\mathrm{SP}(m)}$	Normalized speed of the m-th RIS element relative to the agent
$A^{(m)}(f)$	Amplitude response of the m-th RIS element	$\Phi^{(m)}(f)$	Phase response of the m-th RIS element
$\zeta^{\mathrm{RIS}(m)}$	Area of the m-th RIS element	$\boldsymbol{J}_j(\boldsymbol{p})$	FIM on localization error from paths between the agent and the j-th anchor
$\boldsymbol{J}_j^{\mathrm{DP}}(\boldsymbol{p})$	FIM on localization error from the direct path between the agent and the j-th anchor	$\boldsymbol{J}_j^{(m,m')}(\boldsymbol{p})$	FIM on localization error from the signal coupling of the scattering paths starting at the j-th anchor via the m-th and m'-th RIS elements
$\mathring{\boldsymbol{J}}_j^{\mathrm{D}(m,m')}(\boldsymbol{p})$	FIM on localization error from the signal coupling of the scattering paths starting at the j-th anchor via the m-th and m'-th RIS elements with Doppler shifts	$\mathring{\boldsymbol{J}}_j^{\mathrm{V}(m,m')}(\boldsymbol{p})$	FIM on localization error from the signal coupling of the scattering paths starting at the j-th anchor via the m-th and m'-th RIS elements induced by the RIS velocity
$\boldsymbol{J}_j^{\mathrm{SA}}(\boldsymbol{p})$	FIM on localization error from the signal transmitted by the j-th anchor with a synthetic RIS	$\boldsymbol{\Delta}_j(\boldsymbol{p})$	Difference between FIMs on localization error from the scattering paths starting at the j-th anchor via dynamic large-aperture and synthetic RISs
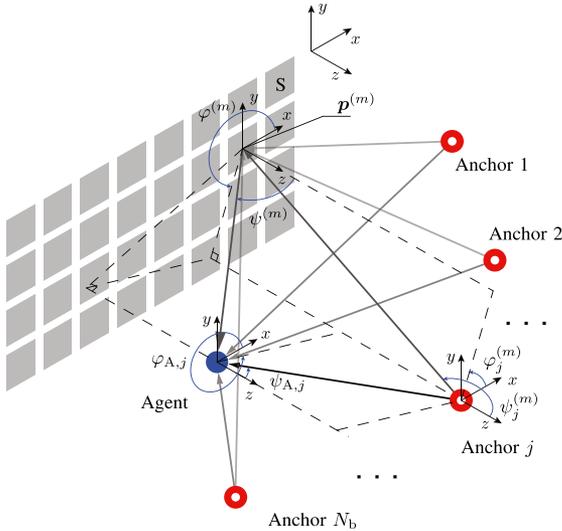
Fig. 1. Localization system with a static wideband RIS. The wideband RIS can control the phase response of each element, therefore, the coupling degree of the scattered wideband signals is adjustable.

with

$$\chi_j = \begin{cases} 1, & \text{for line-of-sight} \\ 0, & \text{for non-line-of-sight} \end{cases}$$

for any t within an observation interval $[0, T_{\mathrm{obs}})$. In (1), $r_j^{\mathrm{DP}}(t)$ and $r_j^{\mathrm{RIS}(m)}(t)$ are the signals received at the agent from the j-th anchor via the direct path and the RIS-scattering path of the element m, and $\mathsf{z}_j(t)$ is a white Gaussian noise with power spectral density (PSD) $N_0/2$.

In the rest of this section, we provide the specific expressions of the signals $r_j^{\mathrm{DP}}(t)$ and $r_j^{\mathrm{RIS}(m)}(t)$, determined by their Fourier transforms $R_j^{\mathrm{DP}}(f)$ and $R_j^{\mathrm{RIS}(m)}(f)$, respectively. The Fourier

transforms are given by

$$R_j^{\mathrm{DP}}(f) = \gamma_j^{\mathrm{DP}} \sqrt{A_j^{\mathrm{DP}}(f) G_j^{\mathrm{DP}}(f)}\, S(f) \alpha_j^{\mathrm{DP}} e^{-j2\pi f \tau_j^{\mathrm{DP}}} \tag{2}$$

$$\begin{aligned} R_j^{\mathrm{RIS}(m)}(f) = {}& \gamma_j^{\mathrm{RIS}(m)} \sqrt{A^{\mathrm{RIS}(m)}(f) G_j^{\mathrm{RIS}(m)}(f)}\, S(f) \\ & \times \alpha_j^{\mathrm{IP}(m)} \alpha^{\mathrm{SP}(m)} e^{-j2\pi f \left(\tau_j^{\mathrm{IP}(m)} + \tau^{\mathrm{SP}(m)}\right)} \\ & \times A_j^{(m)}(f) e^{j\Phi_j^{(m)}(f)} \end{aligned} \tag{3}$$

in which $S(f)$ is the Fourier transform of the transmitted signal $s(t)$ whose bandwidth is much greater than the reciprocal of the observation duration; $A_j^{\mathrm{DP}}(f)$ and $A^{\mathrm{RIS}(m)}(f)$ are the apertures of the Rx antenna at the agent along the direction of the direct path from the j-th anchor and the scattering path via the m-th RIS element, respectively, given by

$$A_j^{\mathrm{DP}}(f) = \frac{\lambda^2}{4\pi} \eta^{\mathrm{Rx}}(f) D^{\mathrm{Rx}}\big(\psi_{\mathrm{A},j}, \varphi_{\mathrm{A},j}\big)$$

$$A^{\mathrm{RIS}(m)}(f) = \frac{\lambda^2}{4\pi} \eta^{\mathrm{Rx}}(f) D^{\mathrm{Rx}}\big(\psi_A^{(m)}, \varphi_A^{(m)}\big)$$

where the wavelength $\lambda = c/f$, and c is the speed of light;[2] $\eta^{\mathrm{Rx}}(f)$ denotes the Rx antenna efficiency, $D^{\mathrm{Rx}}(\psi, \varphi)$ denotes the directivity of the Rx antenna; $G_j^{\mathrm{DP}}(f)$ and $G_j^{\mathrm{RIS}(m)}(f)$ are the gains of the Tx antenna at the j-th anchor along the directions of the direct path and the scattering path via the m-th RIS element, respectively, given by

$$G_j^{\mathrm{DP}}(f) = \eta_j^{\mathrm{Tx}}(f) D_j^{\mathrm{Tx}}\big(\psi_j, \varphi_j\big)$$

---

[2]Note that the wavelength λ is a variable over the wavelength interval corresponding to the considered frequency band, but not the center wavelength λ_c of the transmitted signal.

$$G_j^{\mathrm{RIS}(m)}(f) = \eta_j^{\mathrm{Tx}}(f) D_j^{\mathrm{Tx}}\big(\psi_j^{(m)}, \varphi_j^{(m)}\big)$$

where $\eta_j^{\mathrm{Tx}}(f)$ denotes the Tx antenna efficiency at the j-th anchor, and $D_j^{\mathrm{Tx}}(\psi, \varphi)$ denotes the directivity of the Tx antenna at the j-th anchor; α_j^{DP} and τ_j^{DP} denote the attenuation and delay of the direct path from the j-th anchor to the agent, respectively; $\alpha_j^{\mathrm{IP}(m)}$ and $\tau_j^{\mathrm{IP}(m)}$ denote the attenuation and delay of the incidence path from the j-th anchor to the m-th RIS element, respectively; $\alpha^{\mathrm{SP}(m)}$ and $\tau^{\mathrm{SP}(m)}$ denote the attenuation and delay of the reflection path from the m-th RIS element to the agent, respectively; γ_j^{DP} and $\gamma_j^{\mathrm{RIS}(m)}$ denote the polarization coefficients of the direct path and the scattering path via the m-th RIS element, respectively, given by

$$\gamma_j^{\mathrm{DP}} = \langle \boldsymbol{p} \rightarrow \boldsymbol{p}_j | \boldsymbol{p}_j \rightarrow \boldsymbol{p} \rangle$$

$$\gamma_j^{\mathrm{RIS}(m)} = \langle \boldsymbol{p}^{(m)} \rightarrow \boldsymbol{p} | \boldsymbol{\mathcal{P}}_{\mathrm{RIS}(m)} | \boldsymbol{p}_j \rightarrow \boldsymbol{p}^{(m)} \rangle$$

where the operator $\boldsymbol{\mathcal{P}}_{\mathrm{RIS}(m)}$ denotes the polarization manipulation of the m-th RIS element;[3] $A_j^{(m)}(f)$ and $\Phi_j^{(m)}(f)$ are the amplitude [44] and phase [45] responses of the m-th RIS element along the path from the k-th transmitter, through the element, to the j-th receiver, respectively, given by

$$A_j^{(m)}(f) = \frac{\zeta_j^{\mathrm{RIS}(m)}}{\lambda} \eta^{\mathrm{RIS}}(f)$$

$$\Phi_j^{(m)}(f) = \Phi_{\mathrm{dyn},j}^{(m)}(f) + \Phi_{\mathrm{func},j}^{(m)}(f)$$

where $\zeta_j^{\mathrm{RIS}(m)}/\lambda$ is the effective aperture of the m-th RIS element for incidence EM wave with wavelength λ, and $\eta^{\mathrm{RIS}}(f)$ is the scattering efficiency over the concerned frequency band; $\Phi_{\mathrm{dyn},j}^{(m)}(f)$ is the dynamic phase response caused by the propagation in the m-th RIS element, and $\Phi_{\mathrm{func},j}^{(m)}(f)$ is the functional phase response of the m-th RIS element which can be controlled in the concerned frequency band. The wideband RIS is a real system, so $\Phi_j^{(m)}(-f) = -\Phi_j^{(m)}(f)$ and $A_j^{(m)}(f) = A_j^{(m)}(-f)$.

Consider that the wideband RIS is angle-insensitive, i.e., $\Phi_j^{(m)}(f) = \Phi^{(m)}(f)$ and $\zeta_j^{\mathrm{RIS}(m)} = \zeta^{\mathrm{RIS}(m)}$. Note that even if the positive part $\Phi_+^{(m)}(f)$ of $\Phi^{(m)}(f)$ is a continuous function of frequency,[4] it can be expressed as a finite-order polynomial and controlled in a discrete way, i.e.,

$$\Phi_+^{(m)}(f) = \sum_{k=0}^{K} \Phi_k^{(m)} f^k$$

where the order K is a nonnegative integer, and the controllable parameters satisfy that $\Phi_0^{(m)} \in [0, 2\pi)$ and $d\Phi_+^{(m)}/df \leqslant 0$. Notice that the phase response of the RIS is not assumed to configure different frequency components independently. For example, if the positive part $\Phi_+^{(m)}(f)$ is a first-order polynomial, the degree of freedom (DOF) for configuring the phase response of the m-th RIS element over the considered frequency band is 2. As

---

[3] In this context, the operator can be viewed as a linear mapping from $\mathbb{C}^3$ to $\mathbb{C}^3$, and thus can be represented by a 3-by-3 complex matrix.

[4] $\Phi_+^{(m)}(f) = \Phi^{(m)}(f), \forall f > 0$.
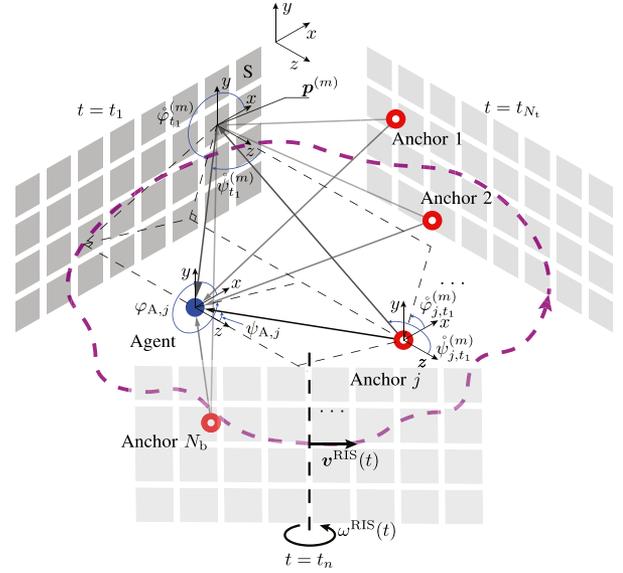
Fig. 2. Localization system with a dynamic/synthetic wideband RIS. For practical applications, the dynamic RISs can be deployed on vehicles patrolling densely populated areas, such as mobile robots and unmanned aerial vehicles.

a result, the phase responses of different frequency components follow an affine relationship and are not independent.

In the proposed model, the EM wave impinging on the static RIS has spherical wavefront. In particular, for each RIS element $m \in \mathcal{N}_\mathrm{s}$, the delays $\tau_j^{\mathrm{IP}(m)}$ and $\tau^{\mathrm{SP}(m)}$ of the scattered signal component are, respectively, given by $\tau_j^{\mathrm{IP}(m)} = \|\boldsymbol{p}^{(m)} - \boldsymbol{p}_j\|/c$ and $\tau^{\mathrm{SP}(m)} = \|\boldsymbol{p} - \boldsymbol{p}^{(m)}\|/c$.

B. Wideband Signal Model for Dynamic RISs

Consider a dynamic RIS in the system described in Fig. 2, where a mild assumption on dynamic RISs is introduced in Assumption 1 to simplify the signal model. A localization system with dynamic RISs implies that a localization measurement is carried out within a single observation interval. Position information from a system with a synthetic RIS is synthesized from measurements taken with a dynamic RIS over multiple observation intervals.

Assumption 1 (Quasi-static and quasi-uniform-speed assumption): For any $m \in \mathcal{N}_{\mathrm{s},t_0}$, the velocity $\mathring{\boldsymbol{v}}^{(m)}(t)$ of the RIS m-th element satisfies

$$\lambda_\mathrm{c} \gg \max_{m \in \mathcal{N}_{\mathrm{s},t_0}} \left\| \int_{t_0}^{t_0+T_\mathrm{obs}} \mathring{\boldsymbol{v}}^{(m)}(t) dt \right\|, \quad \forall t_0 \in \mathbb{R} \quad (4)$$

$$\left\| \mathring{\boldsymbol{v}}_{t_0}^{(m)} \right\| \gg \max_{t,t' \in [t_0, t_0+T_\mathrm{obs})} \left\| \mathring{\boldsymbol{v}}^{(m)}(t) - \mathring{\boldsymbol{v}}^{(m)}(t') \right\|, \quad \forall t_0 \in \mathbb{R} \quad (5)$$

where the vector $\mathring{\boldsymbol{v}}_t^{(m)}$ is the average velocity of the m-th RIS element during the observation interval $[t, t + T_\mathrm{obs})$, and $\mathcal{N}_{\mathrm{s},t}$ is the set of the dynamic RIS elements during the observation interval $[t, t + T_\mathrm{obs})$.

Remark 1: Assumption 1 ensures that the wireless channel with a dynamic RIS is time-invariant during an observation interval. With the center frequency in the GHz regime, Assumption 1 is readily achievable. For a localization system with a center

$$\mathring{R}_j^{\mathrm{RIS}(m)}(f) = \mathring{\gamma}_j^{\mathrm{RIS}(m)} \sqrt{\mathring{A}^{\mathrm{RIS}(m)}(f)\,\mathring{G}_j^{\mathrm{RIS}(m)}\left(f\frac{1-\mathring{\nu}_j^{\mathrm{IP}(m)}}{1-\mathring{\nu}^{\mathrm{SP}(m)}}\right)}\,A^{(m)}\left(f\frac{1}{1-\mathring{\nu}^{\mathrm{SP}(m)}}\right)\exp\left\{j\mathring{\Phi}^{(m)}\left(f\frac{1}{1-\mathring{\nu}^{\mathrm{SP}(m)}}\right)\right\}$$

$$\times\;\mathring{\alpha}_j^{\mathrm{IP}(m)}\mathring{\alpha}^{\mathrm{SP}(m)}S\left(f\frac{1-\mathring{\nu}_j^{\mathrm{IP}(m)}}{1-\mathring{\nu}^{\mathrm{SP}(m)}}\right)\exp\left\{-j2\pi f\left(\mathring{\tau}_j^{\mathrm{IP}(m)}\frac{1-\mathring{\nu}_j^{\mathrm{IP}(m)}}{1-\mathring{\nu}^{\mathrm{SP}(m)}}+\mathring{\tau}^{\mathrm{SP}(m)}\frac{1}{1-\mathring{\nu}^{\mathrm{SP}(m)}}\right)\right\} \tag{6}$$

frequency of $5\,\mathrm{GHz}$ and an observation duration of $66.67\,\mu s$ [46], an average RIS speed of $9\,\mathrm{m/s}$ satisfies the condition (4); and an average acceleration of $10^4\,\mathrm{m/s}^2$ satisfies the condition (5). Therefore, mobile vehicles in complex wireless environments where RISs can be deployed, such as industrial mobile robots and unmanned aerial vehicles, satsify with Assumption 1 [47], [48], [49].

Under Assumption 1, the position and velocity of elements on the dynamic RIS can be considered as constant vectors during the observation interval $[t_0,\, t_0 + T_{\mathrm{obs}})$, i.e., for all $t \in [t_0,\, t_0 + T_{\mathrm{obs}})$ and $m \in \mathcal{N}_{\mathrm{s},t_0}$, it holds that $\mathring{p}^{(m)}(t) = \mathring{p}_{t_0}^{(m)}$ and $\mathring{v}^{(m)}(t) = \mathring{v}_{t_0}^{(m)}$. If $t_0 = 0$, the subscripts of the time-varying scalar $\mathring{x}_0$, vector $\mathring{x}_0$, and set $\mathring{\mathcal{X}}_0$ can be omitted.

The received signal at the agent from the j-th anchor is

$$\mathsf{r}_j(t) = \mathring{\chi}_j r_j^{\mathrm{DP}}(t) + \sum_{m\in\mathring{\mathcal{N}}_{\mathrm{s}}}\tilde{r}_j^{\mathrm{RIS}(m)}(t) + \mathsf{z}_j(t)$$

for any t within the observation interval $[0,\,T_{\mathrm{obs}})$, where the ring on the top of χ_j denotes that the line-of-sight (LOS) condition between the j-th anchor and the agent can vary with time, and the scattered signal component $\tilde{r}_j^{\mathrm{RIS}(m)}(t)$ from the m-th element of the dynamic RIS is given by

$$\tilde{r}_j^{\mathrm{RIS}(m)}(t) = \int_{-\infty}^{\infty}\mathring{R}_j^{\mathrm{RIS}(m)}(f)\,e^{j2\pi ft}df\,.$$

Under Assumption 1, $\mathring{R}_j^{\mathrm{RIS}(m)}(f)$ can be interpreted as the Fourier transform of the received signal over the observation interval $[0,\,T_{\mathrm{obs}})$, given by (6) shown at the top of this page, where the time-varying versions of $\gamma_j^{\mathrm{RIS}(m)}, A^{\mathrm{RIS}(m)}, G_j^{\mathrm{RIS}(m)}, \alpha_j^{\mathrm{IP}(m)}, \alpha^{\mathrm{SP}(m)}, \tau_j^{\mathrm{IP}(m)}$, and $\tau^{\mathrm{SP}(m)}$ are defined by replacing the static $\boldsymbol{p}^{(m)}$, $m \in \mathcal{N}_{\mathrm{s}}$, in the expressions with the time-varying $\mathring{\boldsymbol{p}}_{t_0}^{(m)}$, $m \in \mathcal{N}_{\mathrm{s}}$, at $t_0 = 0$.[5] Specifically, the polarization coefficient, aperture at the agent, and the gain at the j-th anchor over the scattering path via the m-th RIS element are respectively given by

$$\mathring{\gamma}_j^{\mathrm{RIS}(m)} = \langle\mathring{\boldsymbol{p}}^{(m)}\!\to\!\boldsymbol{p}\,|\,\mathring{\mathcal{P}}_{\mathrm{RIS}(m)}\,|\,\boldsymbol{p}_j\!\to\!\mathring{\boldsymbol{p}}^{(m)}\rangle$$

$$\mathring{A}^{\mathrm{RIS}(m)}(f) = \frac{\lambda^2}{4\pi}\eta^{\mathrm{Rx}}(f)D^{\mathrm{Rx}}\big(\mathring{\psi}_{\mathrm{A}}^{(m)},\mathring{\varphi}_{\mathrm{A}}^{(m)}\big)$$

$$\mathring{G}_j^{\mathrm{RIS}(m)}(f) = \eta_j^{\mathrm{Tx}}(f)D_j^{\mathrm{Tx}}\big(\mathring{\psi}_j^{(m)},\mathring{\varphi}_j^{(m)}\big)$$

where $\mathring{\mathcal{P}}_{\mathrm{RIS}(m)}$ denotes the polarization manipulation of the m-th dynamic RIS element. In addition, the relative speeds $\mathring{\nu}^{\mathrm{SP}(m)}$

---

[5]Similar to Section II-A, the EM wave impinging on the dynamic RIS also has spherical wavefront.

and $\mathring{\nu}_j^{\mathrm{IP}(m)}$ in (6) are normalized by the speed of light, given by

$$\mathring{\nu}^{\mathrm{SP}(m)} = \frac{\langle\mathring{\boldsymbol{v}}^{(m)},\boldsymbol{p}-\mathring{\boldsymbol{p}}^{(m)}\rangle}{c\,\|\boldsymbol{p}-\mathring{\boldsymbol{p}}^{(m)}\|}$$

$$\mathring{\nu}_j^{\mathrm{IP}(m)} = \frac{\langle\mathring{\boldsymbol{v}}^{(m)},\mathring{\boldsymbol{p}}^{(m)}-\boldsymbol{p}_j\rangle}{c\,\|\mathring{\boldsymbol{p}}^{(m)}-\boldsymbol{p}_j\|}$$

and the positive part $\mathring{\Phi}_+^{(m)}(f)$ of the RIS phase response $\mathring{\Phi}^{(m)}(f)$ over the interval $[0,\,T_{\mathrm{obs}}]$ can be expressed in a finite-order polynomial form, i.e., $\mathring{\Phi}_+^{(m)}(f) = \sum_{k=0}^{K}\mathring{\Phi}_k^{(m)}f^k$. Note that for multiple observations, the phase response of the RIS should be made time-varing in different time intervals to compensate the motion of the RIS.

C. Location Estimation and Squared Position Error Bound (SPEB)

The received waveform $\mathsf{r}_j(t)$ at the agent from the j-th anchor can be represented by $\boldsymbol{r}_j$ from the Karhunen-Loève expansion. Therefore, all the received waveforms can be represented by a vector $\boldsymbol{r}$, defined as

$$\boldsymbol{r} = \begin{bmatrix}\boldsymbol{r}_1^{\mathrm{T}} & \boldsymbol{r}_2^{\mathrm{T}} & \cdots & \boldsymbol{r}_{N_{\mathrm{b}}}^{\mathrm{T}}\end{bmatrix}^{\mathrm{T}}$$

Moreover, the Fisher information matrix (FIM) is defined as

$$\boldsymbol{J}(\boldsymbol{p}) = \mathbb{E}\left\{\left[\frac{\partial\ln f(\mathsf{r}|\boldsymbol{p})}{\partial\boldsymbol{p}}\right]\left[\frac{\partial\ln f(\mathsf{r}|\boldsymbol{p})}{\partial\boldsymbol{p}}\right]^{\mathrm{T}}\right\} \tag{7}$$

where the expectation is computed over r. The likelihood function $f(\boldsymbol{r}|\boldsymbol{p})$ of all received waveforms can be expressed, due to the independence of the Txs and the implicit multiple access mechanism, as $f(\boldsymbol{r}|\boldsymbol{p}) = \prod_{j=1}^{N_{\mathrm{b}}}f(\boldsymbol{r}_j|\boldsymbol{p})$, where for static RISs, the likelihood function $f(\boldsymbol{r}_j|\boldsymbol{p})$ satisfies

$$f(\boldsymbol{r}_j|\boldsymbol{p}) \propto \exp\left\{-\frac{1}{N_0}\int_0^{T_{\mathrm{obs}}}\Big[r_j(t) - \chi_j r_j^{\mathrm{DP}}(t)\right.$$
$$\left.-\sum_{m\in\mathcal{N}_{\mathrm{s}}}r_j^{\mathrm{RIS}(m)}(t)\Big]^2 dt\right\} \tag{8}$$

and for dynamic RISs, the scalar χ_j, the set $\mathcal{N}_{\mathrm{s}}$, and the signal component $r_j^{\mathrm{RIS}(m)}(t)$ on the right hand side of (8) are replaced by $\mathring{\chi}_j$, $\mathring{\mathcal{N}}_{\mathrm{s}}$, and $\tilde{r}_j^{\mathrm{RIS}(m)}(t)$, respectively. The mean square error of any unbiased estimator $\hat{\mathsf{p}}$ of the parameter vector $\hat{\mathsf{p}}$ satisfies

$$\mathbb{E}\left\{(\hat{\mathsf{p}}-\boldsymbol{p})(\hat{\mathsf{p}}-\boldsymbol{p})^{\mathrm{T}}\right\} \succeq \boldsymbol{J}(\boldsymbol{p})^{-1}$$

where the trace of the right hand side is defined as SPEB [50].

III. DERIVATION OF FIM

This section performs Fisher information analysis based on the proposed wideband signal models. Furthermore, special scenarios including CC and CD scenarios are studied.

A. Wideband Localization With Static RISs

The following lemma presents FIM for estimating an unknown parameter vector $\boldsymbol{\theta}$ based on a real signal $r(t, \boldsymbol{\theta})$.

Lemma 1 (FIM representation in frequency domain): The FIM on the parameter vector $\boldsymbol{\theta}$ of a real time-domain signal $r(t, \boldsymbol{\theta})$ with an additive white Gaussian noise whose PSD is $N_0/2$ can be represented as

$$\boldsymbol{J}(\boldsymbol{\theta}) = \frac{2}{N_0} \int_{-\infty}^{\infty} \frac{\partial R(f, \boldsymbol{\theta})}{\partial \boldsymbol{\theta}} \frac{\partial R^*(f, \boldsymbol{\theta})}{\partial \boldsymbol{\theta}^{\mathrm{T}}} df \tag{9}$$

where $R(f, \boldsymbol{\theta}) = \mathscr{F}\{r(t, \boldsymbol{\theta})\}$.

Proof: See Appendix A in [51]. $\boxtimes$

Definition 1 (Completely coupled): Two signal components $r_1(t), r_2(t)$ are called completely coupled if

$$R_1(f)R_2(f)^* = |R_1(f)||R_2(f)|, \quad \forall f \in \mathbb{R}$$

where $R_1(f) = \mathscr{F}\{r_1(t)\}$ and $R_2(f) = \mathscr{F}\{r_2(t)\}$.

Definition 2 (Completely decoupled): Two signal components $r_1(t, \boldsymbol{\theta}), r_2(t, \boldsymbol{\theta})$ are called completely decoupled if the FIM $\boldsymbol{J}_{12}(\boldsymbol{\theta})$ for estimating the parameter vector $\boldsymbol{\theta}$ from the coupling of the two components is zero, i.e.,

$$\boldsymbol{J}_{12}(\boldsymbol{\theta}) = \frac{2}{N_0} \int_0^{T_{\mathrm{obs}}} \frac{\partial r_1(t, \boldsymbol{\theta})}{\partial \boldsymbol{\theta}} \frac{\partial r_2(t, \boldsymbol{\theta})}{\partial \boldsymbol{\theta}^{\mathrm{T}}} dt = \boldsymbol{0}.$$

Remark 2: The concept of completely coupled signal components can be interpreted as signal components with the same phase spectra. The concept of completely decoupled signal components can be interpreted as independent signal components, where there is no overlap in the estimation information extracted from the different signal components. For example, two signal components carried by independent resource elements in the time-frequency resource grid of an orthogonal frequency division multiplexing (OFDM) system are completely decoupled.

Definition 3 (Coupling kernel matrix (CKM)): We define a CKM to describe the coupling controlled by a static RIS as

$$\boldsymbol{K}(R_1, R_2) =$$
$$\int_{-\infty}^{\infty} \begin{bmatrix} f^2 R_1(f) R_2^*(f) & -\jmath f R_1(f) R_2^*(f) \mathbf{1}_3^{\mathrm{T}} \\ \jmath f R_1(f) R_2^*(f) \mathbf{1}_3 & R_1(f) R_2^*(f) \mathbf{1}_{3 \times 3} \end{bmatrix} df$$

where $R_1(f)$ and $R_2(f)$ denote the Fourier transforms of the transmitted signals via two paths. Each of the two paths can be either a direct path or a scattering path via an RIS element.

Remark 3: The CKM reveals the coupling degree of signal components via different paths. It is worthy to note that the control of phase spectra of signal components exerted by the RIS is reflected in the FIM through the manipulation of the CKMs. The properties of CKMs in special coupling states are as follows:

1) If $R_1(f)$ and $R_2(f)$ are completely coupled, the CKM $\boldsymbol{K}$ is denoted by $\boldsymbol{K}^{\mathrm{C}}$ and is given by

$$\boldsymbol{K}^{\mathrm{C}}(R_1, R_2) =$$
$$\int_{-\infty}^{\infty} \begin{bmatrix} f^2 |R_1(f)||R_2(f)| & \boldsymbol{0}_3^{\mathrm{T}} \\ \boldsymbol{0}_3 & |R_1(f)||R_2(f)| \mathbf{1}_{3 \times 3} \end{bmatrix} df \tag{10}$$

Specially, if $R_1(f) = R_2(f) = R(f)$, the CKM $\boldsymbol{K}$ is denoted by $\boldsymbol{K}^{\mathrm{S}}$ and reduces to

$$\boldsymbol{K}^{\mathrm{S}}(R) = \int_{-\infty}^{\infty} \begin{bmatrix} f^2 |R(f)|^2 & \boldsymbol{0}_3^{\mathrm{T}} \\ \boldsymbol{0}_3 & |R(f)|^2 \mathbf{1}_{3 \times 3} \end{bmatrix} df. \tag{11}$$

2) If $R_1(f)$ and $R_2(f)$ are completely decoupled, the CKM is given by

$$\boldsymbol{K}(R_1, R_2) = \boldsymbol{0}_{4 \times 4}. \tag{12}$$

3) For any $R_1(f), R_2(f)$, it holds that

$$\boldsymbol{K}(R_1, R_2) = \boldsymbol{K}(R_2, R_1)^{\mathrm{T}}.$$

Definition 4 (Information gain vector for the direct path): We define the information gain vector $\boldsymbol{g}_j^{\mathrm{DP}}$ for the direct path between the j-th anchor and the agent as

$$\boldsymbol{g}_j^{\mathrm{DP}} = \begin{bmatrix} 2\pi/c \\ \frac{\partial}{\partial \psi_j} D_j^{\mathrm{Tx}}/(2D_j^{\mathrm{Tx}}) - \frac{\partial}{\partial \psi_{\mathrm{A},j}} D_j^{\mathrm{Rx}}/(2D_j^{\mathrm{Rx}}) \\ \frac{\partial}{\partial \varphi_j} D_j^{\mathrm{Tx}}/(2D_j^{\mathrm{Tx}}) + \frac{\partial}{\partial \varphi_{\mathrm{A},j}} D_j^{\mathrm{Rx}}/(2D_j^{\mathrm{Rx}}) \\ 1/\alpha_j^{\mathrm{DP}} \end{bmatrix}$$

where D_j^{Tx} and D_j^{Rx} are the short forms of $D_j^{\mathrm{Tx}}(\psi_j, \varphi_j)$ and $D^{\mathrm{Rx}}(\psi_{\mathrm{A},j}, \varphi_{\mathrm{A},j})$, respectively.

Definition 5 (Information gain vector for the scattering path via an RIS element): We define the information gain vector $\boldsymbol{g}_j^{\mathrm{SP}(m)}$ for the scattering path via the m-th RIS element starting from the j-th anchor as

$$\boldsymbol{g}_j^{\mathrm{SP}(m)} = \begin{bmatrix} 2\pi/c \\ \frac{\partial}{\partial \psi_{\mathrm{A}}^{(m)}} D^{\mathrm{Rx}}/(2D^{\mathrm{Rx}}) - \frac{\partial}{\partial \psi^{(m)}} \gamma_j^{\mathrm{RIS}(m)}/\gamma_j^{\mathrm{RIS}(m)} \\ \frac{\partial}{\partial \varphi_{\mathrm{A}}^{(m)}} D^{\mathrm{Rx}}/(2D^{\mathrm{Rx}}) + \frac{\partial}{\partial \varphi^{(m)}} \gamma_j^{\mathrm{RIS}(m)}/\gamma_j^{\mathrm{RIS}(m)} \\ 1/\alpha^{\mathrm{SP}(m)} \end{bmatrix}$$

where D^{Rx} is the short form of $D^{\mathrm{Rx}}(\psi_{\mathrm{A}}^{(m)}, \varphi_{\mathrm{A}}^{(m)})$.

Theorem 1: Based on the proposed signal model in Section II-A, the FIM of the agent is given by

$$\boldsymbol{J}(\boldsymbol{p}) = \sum_{j \in \mathcal{N}_{\mathrm{b}}} \boldsymbol{J}_j(\boldsymbol{p}) \tag{13}$$

where $\boldsymbol{J}_j(\boldsymbol{p})$ is the contribution from the j-th anchor, given by

$$\boldsymbol{J}_j(\boldsymbol{p}) = \chi_j \boldsymbol{J}_j^{\mathrm{DP}}(\boldsymbol{p}) + \sum_{m,m' \in \mathcal{N}_{\mathrm{s}}} \boldsymbol{J}_j^{(m,m')}(\boldsymbol{p}) + \chi_j \sum_{m \in \mathcal{N}_{\mathrm{s}}} \boldsymbol{C}_j^{(m)}(\boldsymbol{p}). \tag{14}$$

Specifically, the matrices $\boldsymbol{J}_j^{\mathrm{DP}}(\boldsymbol{p})$, $\boldsymbol{J}_j^{(m,m')}(\boldsymbol{p})$, and $\boldsymbol{C}_j^{(m)}(\boldsymbol{p})$ are the FIMs from the direct path, from the coupling of scattering paths via RIS elements, and from the coupling of a scattering

path via an RIS element and the direct path, respectively, given by

$$\boldsymbol{J}_j^{\mathrm{DP}}(\boldsymbol{p}) = \frac{2}{N_0} \boldsymbol{Q}_j^{\mathrm{DP}} \left[\boldsymbol{K}_j^{\mathrm{DP}} \odot \boldsymbol{W}_j^{\mathrm{DP}} \right] \left(\boldsymbol{Q}_j^{\mathrm{DP}} \right)^{\mathrm{T}} \tag{15}$$

$$\boldsymbol{J}_j^{(m,m')}(\boldsymbol{p}) = \frac{2}{N_0} \boldsymbol{Q}^{\mathrm{SP}(m)} [\boldsymbol{K}_j^{(m,m')} \odot \boldsymbol{W}_j^{(m,m')}] (\boldsymbol{Q}^{\mathrm{SP}(m')})^{\mathrm{T}}, \tag{16}$$

$$\boldsymbol{C}_j^{(m)}(\boldsymbol{p}) = \frac{2}{N_0} \kappa \left(\boldsymbol{Q}_j^{\mathrm{DP}} \left[\boldsymbol{K}_j^{(m)} \odot \boldsymbol{W}_j^{(m)} \right] (\boldsymbol{Q}^{\mathrm{SP}(m)})^{\mathrm{T}} \right) \tag{17}$$

where $\boldsymbol{K}_j^{\mathrm{DP}} = \boldsymbol{K}^{\mathrm{S}}(R_j^{\mathrm{DP}})$, $\boldsymbol{W}_j^{\mathrm{DP}} = \boldsymbol{g}_j^{\mathrm{DP}}(\boldsymbol{g}_j^{\mathrm{DP}})^{\mathrm{T}}$, $\boldsymbol{K}_j^{(m,m')} = \boldsymbol{K}(R_j^{\mathrm{RIS}(m)}, R_j^{\mathrm{RIS}(m')})$, $\boldsymbol{W}_j^{(m,m')} = \boldsymbol{g}_j^{\mathrm{SP}(m)}(\boldsymbol{g}_j^{\mathrm{SP}(m')})^{\mathrm{T}}$, $\boldsymbol{K}_j^{(m)} = \boldsymbol{K}(R_j^{\mathrm{DP}}, R_j^{\mathrm{RIS}(m)})$, $\boldsymbol{W}_j^{(m)} = \boldsymbol{g}_j^{\mathrm{DP}}(\boldsymbol{g}_j^{\mathrm{SP}(m)})^{\mathrm{T}}$, and the Jacobian matrices $\boldsymbol{Q}_j^{\mathrm{DP}}$ and $\boldsymbol{Q}^{\mathrm{RIS}(m)}$ are given by (35) and (36), respectively.

Proof: See Appendix A. $\boxtimes$

Remark 4: In LOS condition, the FIM $\boldsymbol{J}_j(\boldsymbol{p})$ consists of three components: the FIM $\boldsymbol{J}_j^{\mathrm{DP}}(\boldsymbol{p})$ from the direct path, the FIM $\boldsymbol{J}_j^{\mathrm{RIS}}(\boldsymbol{p})$ from the scattering paths, and the FIM $\boldsymbol{C}_j^{\mathrm{DP,RIS}}(\boldsymbol{p})$ from the coupling of the direct path and the scattering paths, where $\boldsymbol{J}_j^{\mathrm{RIS}}(\boldsymbol{p}) = \sum_{m,m' \in \mathcal{N}_\mathrm{s}} \boldsymbol{J}_j^{(m,m')}(\boldsymbol{p})$ and $\boldsymbol{C}_j^{\mathrm{DP,RIS}}(\boldsymbol{p}) = \sum_{m \in \mathcal{N}_\mathrm{s}} \boldsymbol{C}_j^{(m)}(\boldsymbol{p})$. The FIM from the coupling of the direct path and the scattering paths is the sum of the FIMs from the coupling of the direct path and each scattering path. In non-line-of-sight (NLOS) condition, the FIM $\boldsymbol{J}_j^{\mathrm{DP}}(\boldsymbol{p})$ from the direct path and the FIM $\boldsymbol{C}_j^{\mathrm{DP,RIS}}(\boldsymbol{p})$ from the coupling of the direct path and the scattering paths are eliminated. All components of the FIM $\boldsymbol{J}_j(\boldsymbol{p})$ contain CKMs as kernels. The wideband RIS can control the CKMs of $\boldsymbol{J}_j^{\mathrm{RIS}}(\boldsymbol{p})$ and $\boldsymbol{C}_j^{\mathrm{DP,RIS}}(\boldsymbol{p})$.

We now briefly discuss Fisher information analysis for holographic localization with multiple agents. Multi-agent holographic localization can be categorized as noncooperative, spatial cooperative, and spatio-temporal cooperative cases, where the FIM in Theorem 1 can be generalized in a similar manner as that illustrated in the Fig. 4 of [46]. For the noncooperative case, the FIM associated to the errors on the positions of agents becomes a block-diagonal matrix and each of its block corresponds to an agent. Specifically, consider N_a agents where the position of the i-th agent is denoted by $\boldsymbol{p}_i^\mathrm{a}$, $i \in \{1, 2, \ldots, N_\mathrm{a}\}$. Then, the FIM of all agents is given by

$$\mathrm{diag}\{\boldsymbol{J}(\boldsymbol{p}_1^\mathrm{a}), \boldsymbol{J}(\boldsymbol{p}_2^\mathrm{a}), \ldots, \boldsymbol{J}(\boldsymbol{p}_{N_\mathrm{a}}^\mathrm{a})\}$$

where $\boldsymbol{J}(\boldsymbol{p}_i^\mathrm{a})$ is given by (13) with $\boldsymbol{p}$ replaced by $\boldsymbol{p}_i^\mathrm{a}$. For the spatial and spatio-temporal cooperative cases, the cooperation increases the diagonal blocks in terms of positive-semidefiniteness and makes off-diagonal blocks non-zero.

B. Wideband Localization in Complete Coupling/Decoupling Scenarios

To further illustrate how Fisher information is affected by a wideband RIS, two types of scenarios, namely, CC scenarios and CD scenarios, are evaluated.

Corollary 1 (CC scenario): If all signal components via scattering paths are completely coupled, and any signal component

via a scattering path and the signal component via the direct path are completely decoupled, then the FIM of the agent contributed by the j-th anchor is given by

$$\boldsymbol{J}_j(\boldsymbol{p}) = \chi_j \boldsymbol{J}_j^{\mathrm{DP}}(\boldsymbol{p}) + \sum_{m,m' \in \mathcal{N}_\mathrm{s}} \boldsymbol{J}_j^{\mathrm{C}(m,m')}(\boldsymbol{p})$$

where $\boldsymbol{J}_j^{\mathrm{DP}}(\boldsymbol{p})$ is given by (15), and $\boldsymbol{J}_j^{\mathrm{C}(m,m')}(\boldsymbol{p})$ is given by

$$\frac{2}{N_0} \boldsymbol{Q}^{\mathrm{SP}(m)} [\boldsymbol{K}^{\mathrm{C}}(R_j^{\mathrm{RIS}(m)}, R_j^{\mathrm{RIS}(m')}) \odot \boldsymbol{W}_j^{(m,m')}] (\boldsymbol{Q}^{\mathrm{SP}(m')})^{\mathrm{T}}$$

with $\boldsymbol{W}_j^{(m,m')} = \boldsymbol{g}_j^{\mathrm{SP}(m)}(\boldsymbol{g}_j^{\mathrm{SP}(m')})^{\mathrm{T}}$.

Proof: Apply (10) and (11) to Theorem 1. $\boxtimes$

Corollary 2 (CD scenario): If all signals via different paths are completely decoupled, then the FIM of the agent contributed by the j-th anchor is given by

$$\boldsymbol{J}_j(\boldsymbol{p}) = \chi_j \boldsymbol{J}_j^{\mathrm{DP}}(\boldsymbol{p}) + \sum_{m=1}^{N_\mathrm{s}} \boldsymbol{J}_j^{(m,m)}(\boldsymbol{p})$$

where $\boldsymbol{J}_j^{\mathrm{DP}}(\boldsymbol{p})$ is given by (15), and $\boldsymbol{J}_j^{(m,m)}(\boldsymbol{p})$ is given by

$$\frac{2}{N_0} \boldsymbol{Q}^{\mathrm{SP}(m)} \left[\boldsymbol{K}^{\mathrm{S}}(\boldsymbol{R}_j^{\mathrm{RIS}(m)}) \odot \boldsymbol{W}_j^{(m,m)} \right] (\boldsymbol{Q}^{\mathrm{SP}(m)})^{\mathrm{T}}$$

with $\boldsymbol{W}_j^{(m,m)} = \boldsymbol{g}_j^{\mathrm{SP}(m)}(\boldsymbol{g}_j^{\mathrm{SP}(m)})^{\mathrm{T}}$.

Proof: Apply (11) and (12) to Theorem 1. $\boxtimes$

Remark 5: By appropriately configuring the wideband RIS, the coupling degree among signal components from the scattering paths can be strengthened or weakened. Moreover, due to the causality property of RISs, the coupling degree between signal components from the direct path and any of the scattering paths can only be weakened. Both CC and CD scenarios eliminate the coupling between the direct path and any scattering path. The difference between these two types of scenarios is the coupling among the scattering paths, i.e., the FIM from the complete coupling among the scattering paths, given by

$$\boldsymbol{C}_j^{\mathrm{RIS}}(\boldsymbol{p}) = \sum_{m=1}^{N_\mathrm{s}} \sum_{\substack{m'=1 \\ m' \neq m}}^{N_\mathrm{s}} \boldsymbol{C}_j^{\mathrm{RIS}(m,m')}(\boldsymbol{p})$$

where $\boldsymbol{C}_j^{\mathrm{RIS}(m,m')}(\boldsymbol{p})$ is the FIM from the coupling of the scattering path via the m-th RIS element and the scattering path via the m'-th RIS element.

C. Wideband Localization With Dynamic RISs

This subsection presents the definitions of frequency-sensitivity, CKMs, and information gain vectors, as well as the FIM and its decomposition for a localization system with a dynamic RIS.

Definition 6 (Frequency-sensitivity of the transmitted waveform): We define the frequency-sensitivity $\tilde{S}(f)$ of the transmitted waveform $S(f)$ in frequency domain as

$$\tilde{S}(f) = \frac{1}{S(f)} \frac{dS(f)}{df}, \qquad f \in \mathrm{supp}(S) \tag{18}$$

where $\mathrm{supp}(S)$ is the support set $\{f \in \mathbb{R} : S(f) \neq 0\}$.

Remark 6: The $\tilde{S}(f)$ in (18) reflects the sensitivity of the frequency-domain waveform $S(f)$ to f. It is worthy to note that

$\jmath \tilde{S}(f)$ and its frequency-scaled version $\jmath \tilde{S}(\alpha f)$ with $\alpha > 0$ have conjugate symmetry if $S(f)$ has conjugate symmetry.

Definition 7 (Velocity-induced CKMs between an RIS-scattering path and a direct path): We define the velocity-induced CKMs between the scattering path via the m-th RIS element and direct path with the j-th anchor as

$$\mathring{\boldsymbol{K}}_{j,t}^{\mathrm{V}(m)}(R_1) = \int \mathring{\boldsymbol{M}}_{j,t}^{(m)}(f) R_1(f) \mathring{R}_{j,t}^{(m)}(f)^* df$$

where the matrix $\mathring{\boldsymbol{M}}_{j,t}^{(m)}(f)$ is given by

$$\begin{bmatrix} -\jmath f^2 \mathring{\tilde{S}}_{j,t}^{(m)}(f)^* & f^2 \mathbf{1}_2^{\mathrm{T}} & -\jmath f \\ f \mathring{\tilde{S}}_{j,t}^{(m)}(f)^* \mathbf{1}_3 & \jmath f \mathbf{1}_{3\times 2} & \mathbf{1}_3 \end{bmatrix}$$

and the frequency-sensitivity $\mathring{\tilde{S}}_{j,t}^{(m)}(f)$ with Doppler shifts on the scattering path via the m-th RIS element can be expressed as $\tilde{S}\left(f \frac{1-\mathring{\nu}_{j,t}^{\mathrm{IP}(m)}}{1-\mathring{\nu}_t^{\mathrm{SP}(m)}} \right)$.

Definition 8 (Velocity-induced CKMs between two RIS-scattering paths): We define the velocity-induced CKMs between the scattering paths via the m-th and m'-th RIS elements as

$$\mathring{\boldsymbol{K}}_{j,t}^{\mathrm{V}(m,m')} = \int \mathring{\boldsymbol{M}}_{j,t}^{(m,m')}(f) \mathring{R}_{j,t}^{(m)}(f) \mathring{R}_{j,t}^{(m')}(f)^* df$$

where the matrix $\mathring{\boldsymbol{M}}_{j,t}^{(m,m')}(f)$ is given by

$$\begin{bmatrix} f^2 \mathring{\tilde{S}}_{j,t}^{(m)}(f) \mathring{\tilde{S}}_t^{(m')}(f)^* & \jmath f^2 \mathring{\tilde{S}}_{j,t}^{(m)}(f) \mathbf{1}_2^{\mathrm{T}} & f \mathring{\tilde{S}}_{j,t}^{(m)}(f) \\ -\jmath f^2 \mathring{\tilde{S}}_{j,t}^{(m')}(f)^* \mathbf{1}_2 & f^2 \mathbf{1}_{2\times 2} & -\jmath f \mathbf{1}_2 \\ f \mathring{\tilde{S}}_{j,t}^{(m')}(f)^* & \jmath f \mathbf{1}_2^{\mathrm{T}} & 1 \end{bmatrix}.$$

Remark 7: The velocity-induced CKMs in Definitions 7 and 8 are only valid when there exists at least one $m_0 \in \mathcal{N}_{\mathrm{s}}$ such that $\mathring{\boldsymbol{v}}^{(m_0)} \neq \mathbf{0}$ during the observation interval.

Similar to Definition 3, velocity-induced CKMs also have properties in special coupling states as follows

1) If $\mathring{R}_j^{(m)}(f)$ and $\mathring{R}_j^{(m')}(f)$, $m, m' \in \mathcal{N}_{\mathrm{s}}$ are completely coupled, the velocity-induced CKM is given by

$$\mathring{\boldsymbol{K}}_{j,t}^{\mathrm{C}(m,m')} = \int \mathring{\boldsymbol{M}}_{j,t}^{\mathrm{C}(m,m')}(f) \mathring{R}_{j,t}^{(m)}(f) \mathring{R}_{j,t}^{(m')}(f)^* df \tag{19}$$

where the matrix $\mathring{\boldsymbol{M}}_{j,t}^{\mathrm{C}(m,m')}(f)$ is given by

$$\begin{bmatrix} f^2 \mathring{\tilde{S}}_{j,t}^{(m)}(f) \mathring{\tilde{S}}_{j,t}^{(m')}(f)^* & \jmath f^2 \mathring{\tilde{S}}_{j,t}^{(m)}(f) \mathbf{1}_2^{\mathrm{T}} & f \mathring{\tilde{S}}_{j,t}^{(m)}(f) \\ -\jmath f^2 \mathring{\tilde{S}}_{j,t}^{(m')}(f)^* \mathbf{1}_2 & f^2 \mathbf{1}_{2\times 2} & \mathbf{0}_2 \\ f \mathring{\tilde{S}}_{j,t}^{(m')}(f)^* & \mathbf{0}_2^{\mathrm{T}} & 1 \end{bmatrix}.$$

Moreover, if $\Im\{S(f)\} = 0$, the matrix $\mathring{\boldsymbol{M}}_{j,t}^{\mathrm{C}(m,m')}(f)$ can be further simplified to

$$\begin{bmatrix} f^2 \mathring{\tilde{S}}_{j,t}^{(m)}(f) \mathring{\tilde{S}}_{j,t}^{(m')}(f) & \mathbf{0}_2^{\mathrm{T}} & f \mathring{\tilde{S}}_{j,t}^{(m)}(f) \\ \mathbf{0}_2 & f^2 \mathbf{1}_{2\times 2} & \mathbf{0}_2 \\ f \mathring{\tilde{S}}_{j,t}^{(m')}(f) & \mathbf{0}_2^{\mathrm{T}} & 1 \end{bmatrix}.$$

Since the RIS cannot affect direct paths, it is impossible for the signal components from a direct path and a scattering path via an RIS element to be completely coupled.

2) If $\mathring{R}_j^{(m)}(f)$ and $\mathring{R}_j^{(m')}(f)$, $m, m' \in \mathcal{N}_{\mathrm{s}}$ are completely decoupled, then

$$\mathring{\boldsymbol{K}}_{j,t}^{\mathrm{V}(m,m')} = \mathbf{0}_{4\times 4} \text{ and } \mathring{\boldsymbol{K}}_j^{\mathrm{V}(m')}(\mathring{R}_j^{(m)}) = \mathbf{0}_{4\times 4} . \tag{20}$$

If $\mathring{R}_j^{\mathrm{DP}}(f)$ and $\mathring{R}_j^{(m)}(f)$, $m \in \mathcal{N}_{\mathrm{s}}$ are completely decoupled, then

$$\mathring{\boldsymbol{K}}_{j,t}^{\mathrm{V}(m)}\left(R_j^{\mathrm{DP}}\right) = \mathbf{0}_{4\times 4} . \tag{21}$$

3) The veclocity-induced CKMs in Definition 8 satisfy

$$\mathring{\boldsymbol{K}}_{j,t}^{(m,m')} = \left(\mathring{\boldsymbol{K}}_{j,t}^{(m',m)}\right)^{\mathrm{T}}, \forall m, m' \in \mathcal{N}_{\mathrm{s}} .$$

Definition 9 (Doppler-shifted information gain vector for the scattering path): The Doppler-shifted gain vector $\mathring{\boldsymbol{q}}_t^{\mathrm{SP}(m)}$ for the scattering path via the m-th RIS element at the observation interval $[t, t + T_{\mathrm{obs}})$ is defined as

$$\mathring{\boldsymbol{g}}_{j,t}^{\mathrm{D}(m)} = \begin{bmatrix} 2\pi / \left(c(1 - \mathring{\nu}_t^{(m)})\right) \\ \frac{\partial}{\partial \mathring{\psi}_{\mathrm{A},t}^{(m)}} \mathring{D}_t^{\mathrm{Rx}} / \left(2\mathring{D}_t^{\mathrm{Rx}}\right) - \frac{\partial}{\partial \mathring{\psi}_t^{(m)}} \mathring{\gamma}_{j,t}^{\mathrm{RIS}(m)} / \mathring{\gamma}_{j,t}^{\mathrm{RIS}(m)} \\ \frac{\partial}{\partial \mathring{\varphi}_{\mathrm{A},t}^{(m)}} \mathring{D}_t^{\mathrm{Rx}} / \left(2\mathring{D}_t^{\mathrm{Rx}}\right) + \frac{\partial}{\partial \mathring{\varphi}_t^{\mathrm{SP}(m)}} \mathring{\gamma}_{j,t}^{\mathrm{RIS}(m)} / \mathring{\gamma}_{j,t}^{\mathrm{RIS}(m)} \\ 1/\mathring{\alpha}_t^{\mathrm{SP}(m)} \end{bmatrix}$$

where $\mathring{D}_t^{\mathrm{Rx}}$ is the short form of $D^{\mathrm{Rx}}(\mathring{\psi}_{\mathrm{A},t}^{(m)}, \mathring{\varphi}_{\mathrm{A},t}^{(m)})$.

Definition 10 (Velocity-induced information gain vector for the scattering path): The velocity-induced information gain vector $\mathring{\boldsymbol{g}}_{j,t}^{\mathrm{V}(m)}$ for the scattering path via the m-th RIS element at the observation interval $[t, t + T_{\mathrm{obs}})$ is defined as

$$\mathring{\boldsymbol{g}}_{j,t}^{\mathrm{V}(m)} = \begin{bmatrix} \frac{1-\mathring{\nu}_{j,t}^{\mathrm{IP}(m)}}{(1-\mathring{\nu}_t^{\mathrm{SP}(m)})^2} \\ 2\pi \mathring{\tau}_t^{\mathrm{SP}(m)} \frac{1}{(1-\mathring{\nu}_t^{\mathrm{SP}(m)})^2} \\ 2\pi \mathring{\tau}_t^{\mathrm{IP}(m)} \frac{1-\mathring{\nu}_{j,t}^{\mathrm{IP}(m)}}{(1-\mathring{\nu}_t^{\mathrm{SP}(m)})^2} \\ \frac{1}{1-\mathring{\nu}_t^{\mathrm{SP}(m)}} \end{bmatrix} .$$

Remark 8: If $\mathring{\boldsymbol{v}}_t^{(m)} = \mathbf{0}$, there is no Doppler shift in signal transmission, and thus the gain vector $\mathring{\boldsymbol{q}}_{j,t}^{\mathrm{SP}(m)}$ in Definition 9 reduces to $\boldsymbol{q}_j^{\mathrm{SP}(m)}$ in Definition 5. The gain vector $\mathring{\boldsymbol{g}}_{j,t}^{\mathrm{SP}(m)}$ defined in Definition 10 is valid only if the velocity $\mathring{\boldsymbol{v}}_t^{(m)}$ of the m-th RIS element is not a zero vector.

With the proposed signal model in Section II-B and Definitions 6–10, the FIM for a localization system with a dynamic RIS is given by Theorem 2.

Theorem 2: The FIM $\mathring{\boldsymbol{J}}_j(\boldsymbol{p})$ of the agent contributed by the measurement between the agent and the j-th anchor with a dynamic RIS during the observation interval $[0, T_{\text{obs}})$ is given by

$$\mathring{\boldsymbol{J}}_j(\boldsymbol{p}) = \mathring{\chi}_j \boldsymbol{J}_j^{\text{DP}}(\boldsymbol{p}) + \sum_{m,m' \in \mathring{\mathcal{N}}_{\text{s}}} \mathring{\boldsymbol{J}}_j^{(m,m')}(\boldsymbol{p}) + \mathring{\chi}_j \sum_{m \in \mathring{\mathcal{N}}_{\text{s}}} \mathring{\boldsymbol{C}}_j^{(m)}(\boldsymbol{p}) . \tag{22}$$

In (22), the matrix $\mathring{\boldsymbol{J}}_j^{(m,m')}(\boldsymbol{p})$ can be separated as the Doppler-shifted component $\mathring{\boldsymbol{J}}_j^{\text{D}(m,m')}(\boldsymbol{p})$ and the velocity-induced component $\mathring{\boldsymbol{J}}_j^{\text{V}(m,m')}(\boldsymbol{p})$, i.e.,

$$\mathring{\boldsymbol{J}}_j^{(m,m')}(\boldsymbol{p}) = \mathring{\boldsymbol{J}}_j^{\text{D}(m.m')}(\boldsymbol{p}) + \mathring{\boldsymbol{J}}_j^{\text{V}(m,m')}(\boldsymbol{p}) . \tag{23}$$

In particular,

$$\mathring{\boldsymbol{J}}_j^{\text{D}(m.m')}(\boldsymbol{p}) = \frac{2}{N_0} \mathring{\boldsymbol{Q}}^{\text{D}(m)} \big[\mathring{\boldsymbol{K}}_j^{(m,m')} \odot \mathring{\boldsymbol{W}}_j^{\text{D}(m,m')} \big]$$
$$\times \big(\mathring{\boldsymbol{Q}}^{\text{D}(m')} \big)^{\text{T}} \tag{24}$$

$$\mathring{\boldsymbol{J}}_j^{\text{V}(m,m')}(\boldsymbol{p}) = \frac{2}{N_0} \big(\mathring{\boldsymbol{g}}_j^{\text{V}(m)} \big)^{\text{T}} \mathring{\boldsymbol{K}}_j^{\text{V}(m,m')} \mathring{\boldsymbol{g}}_j^{\text{V}(m)} \mathring{\boldsymbol{q}}^{\text{V}(m)} \big(\mathring{\boldsymbol{q}}^{\text{V}(m')} \big)^{\text{T}}$$
$$+ \frac{2}{N_0} \kappa \Big(\mathring{\boldsymbol{Q}}^{\text{D}(m)} \big[\big(\mathring{\boldsymbol{K}}_j^{\text{V}(m')}(\mathring{R}_j^{(m)}) \mathring{\boldsymbol{g}}_j^{\text{V}(m')} \big)$$
$$\odot \mathring{\boldsymbol{g}}_j^{\text{D}(m)} \big] \big(\mathring{\boldsymbol{q}}^{\text{V}(m')} \big)^{\text{T}} \Big) \tag{25}$$

where $\mathring{\boldsymbol{K}}_j^{(m,m')} = \boldsymbol{K}\big(\mathring{R}_j^{\text{RIS}(m)}(f), \mathring{R}_j^{\text{RIS}(m')}(f) \big)$, $\mathring{\boldsymbol{W}}_j^{\text{D}(m,m')} = \mathring{\boldsymbol{g}}_j^{\text{D}(m)} \big(\mathring{\boldsymbol{g}}_j^{\text{D}(m')} \big)^{\text{T}}$, and the Doppler-shifted Jacobian matrix $\mathring{\boldsymbol{Q}}^{\text{D}(m)}$ and the velocity-induced Jacobian vector $\mathring{\boldsymbol{q}}^{\text{V}(m)}$ are given by (40) and (41), respectively.

Similarly, the matrix $\mathring{\boldsymbol{C}}_j^{(m)}(\boldsymbol{p})$ can be separated as the Doppler-shifted component $\mathring{\boldsymbol{C}}_j^{\text{D}(m)}(\boldsymbol{p})$ and the velocity-induced component $\mathring{\boldsymbol{C}}_j^{\text{V}(m)}(\boldsymbol{p})$, i.e.,

$$\mathring{\boldsymbol{C}}_j^{(m)}(\boldsymbol{p}) = \mathring{\boldsymbol{C}}_j^{\text{D}(m)}(\boldsymbol{p}) + \mathring{\boldsymbol{C}}_j^{\text{V}(m)}(\boldsymbol{p}) . \tag{26}$$

In particular,

$$\mathring{\boldsymbol{C}}_j^{\text{D}(m)}(\boldsymbol{p}) = \frac{2}{N_0} \kappa \Big(\boldsymbol{Q}_j^{\text{DP}} \big[\big(\boldsymbol{g}_j^{\text{DP}} (\mathring{\boldsymbol{g}}^{\text{D}(m)})^{\text{T}} \big) \odot \mathring{\boldsymbol{K}}_j^{(m)} \big]$$
$$\times \big(\mathring{\boldsymbol{Q}}_t^{\text{D}(m)} \big)^{\text{T}} \Big) \tag{27}$$

$$\mathring{\boldsymbol{C}}_j^{\text{V}(m)}(\boldsymbol{p}) = \frac{2}{N_0} \kappa \Big(\boldsymbol{Q}_j^{\text{DP}} \big[\boldsymbol{g}_j^{\text{DP}} \odot \big(\mathring{\boldsymbol{K}}_j^{\text{V}(m)}(R_j^{\text{DP}}) \mathring{\boldsymbol{g}}^{\text{V}(m)} \big) \big]$$
$$\times \big(\mathring{\boldsymbol{q}}_t^{\text{V}(m)} \big)^{\text{T}} \Big) \tag{28}$$

where $\mathring{\boldsymbol{K}}_j^{(m)} = \boldsymbol{K}(R_j^{\text{DP}}, \mathring{R}_j^{\text{RIS}(m)})$.

Proof: See Appendix B. ⊠

Remark 9: The Jacobian vector $\mathring{\boldsymbol{q}}^{\text{V}(m)}$ in (41) can be written as

$$\mathring{\boldsymbol{q}}^{\text{V}(m)} = \frac{\langle \mathring{\boldsymbol{v}}^{(m)}, \boldsymbol{q}_0(\mathring{\psi}^{(m)} + \pi/2, \mathring{\varphi}^{(m)}) \rangle}{c \| \boldsymbol{p} - \mathring{\boldsymbol{p}}^{(m)} \|} \boldsymbol{q}_0\big(\mathring{\psi}^{(m)} + \frac{\pi}{2}, \mathring{\varphi}^{(m)} \big)$$
$$+ \frac{\langle \mathring{\boldsymbol{v}}^{(m)}, \boldsymbol{q}_0(\pi/2, \mathring{\varphi}^{(m)} + \pi/2) \rangle}{c \| \boldsymbol{p} - \mathring{\boldsymbol{p}}^{(m)} \|} \boldsymbol{q}_0\big(\frac{\pi}{2}, \mathring{\varphi}^{(m)} + \frac{\pi}{2} \big)$$

which implies that the velocity components along the connecting lines between the m-th RIS element and the agent have no impact on $\mathring{\boldsymbol{q}}^{\text{V}(m)}$, and its direction is determined by the tangential velocity perpendicular to the connecting lines between the m-th RIS element and the agent.

From the FIM decompositions in (23) and (26), it can be observed that the velocity $\mathring{\boldsymbol{v}}^{(m)}$ of the m-th RIS element affects the FIM in two aspects. First, it introduces Doppler shifts in the information gain vectors and CKMs of the FIM in Theorem 1. Second, the velocity induces new matrices that influence the information intensity in the two angular directions $\boldsymbol{q}_0(\frac{\pi}{2}, \mathring{\varphi}^{(m)} + \frac{\pi}{2})$ and $\boldsymbol{q}_0(\frac{\pi}{2}, \mathring{\varphi}^{(m)} + \frac{\pi}{2})$. It is worthy to note that, if the speed $\| \boldsymbol{v}^{(m)} \|$ of the m-th RIS element tends to zero, the corresponding Doppler-shifted components tend to their counterparts in Theorem 1 and the corresponding velocity-induced components tend to zero matrices.

Corollary 3 (CC scenario): If all signal components via RIS-scattering paths are completely coupled, and any signal component via an RIS-scattering path and the signal component via the direct path are completely decoupled, then the FIM of the agent contributed by the j-th anchor is given by

$$\mathring{\boldsymbol{J}}_j(\boldsymbol{p}) = \mathring{\chi}_j \boldsymbol{J}_j^{\text{DP}}(\boldsymbol{p}) + \sum_{m,m' \in \mathring{\mathcal{N}}_{\text{s}}} \mathring{\boldsymbol{J}}_j^{\text{C}(m,m')}(\boldsymbol{p}) . \tag{}$$

Proof: Apply (19)–(21) to Theorem 2. ⊠

Corollary 4 (CD scenario): If all signals via different paths are completely decoupled, then the FIM of the agent contributed by the j-th anchor is given by

$$\mathring{\boldsymbol{J}}_j(\boldsymbol{p}) = \mathring{\chi}_j \boldsymbol{J}_j^{\text{DP}}(\boldsymbol{p}) + \sum_{m \in \mathring{\mathcal{N}}_{\text{s}}} \mathring{\boldsymbol{J}}_j^{\text{C}(m,m)}(\boldsymbol{p}) . \tag{}$$

Proof: Apply (20) and (21) to Theorem 2. ⊠

D. Synthetic RISs for Network Localization

If the position of the agent is measured at different observation intervals in a localization system with a dynamic RIS, the information obtained from the multiple observations with the dynamic RIS at different locations is equivalent to that provided by a virtual synthetic RIS. Specifically, the FIM of the position of the agent obtained with the virtual synthetic RIS is presented in Theorem 3.

Theorem 3 (FIM with a synthetic RIS): For the j-th anchor, the FIM with a virtual RIS synthesized from the N_{t} observation intervals indexed by $\mathcal{N}_{\text{t}} = \{1, 2, \dots, N_{\text{t}}\}$ is given by

$$\boldsymbol{J}_j^{\text{SA}}(\boldsymbol{p}) = \boldsymbol{J}_j^{\text{DP}}(\boldsymbol{p}) \sum_{n \in \mathcal{N}_{\text{t}}} \mathring{\chi}_{j,t_n} + \sum_{n \in \mathcal{N}_{\text{t}}} \mathring{\boldsymbol{J}}_{j,t_n}^{\text{RIS}}(\boldsymbol{p})$$
$$+ \sum_{n \in \mathcal{N}_{\text{t}}} \mathring{\chi}_{j,t_n} \mathring{\boldsymbol{C}}_{j,t_n}^{\text{DP,RIS}}(\boldsymbol{p}) \tag{29}$$

where $\mathring{\chi}_{j,t_n}$ represents the status of the direct path between the agent and the j-th anchor during the n-th observation interval $[t_n, t_n + T_{\text{obs}})$, $\mathring{\boldsymbol{J}}_{j,t}^{\text{RIS}}(\boldsymbol{p}) = \sum_{m,m' \in \mathring{\mathcal{N}}_{\text{s}}} \mathring{\boldsymbol{J}}_{j,t}^{(m,m')}(\boldsymbol{p})$ and $\mathring{\boldsymbol{C}}_{j,t}^{\text{DP,RIS}}(\boldsymbol{p}) = \sum_{m \in \mathcal{N}_{\text{s}}} \mathring{\boldsymbol{C}}_{j,t}^{(m)}(\boldsymbol{p})$.

Proof: By independence of different observations, we have $\boldsymbol{J}_j^{\text{SA}}(\boldsymbol{p}) = \sum_{n \in \mathcal{N}_{\text{t}}} \mathring{\boldsymbol{J}}_{j,t}(\boldsymbol{p})$. Recall the notation that

$\mathring{\boldsymbol{J}}_{j,0}^{(m,m')} = \mathring{\boldsymbol{J}}_{j}^{(m,m')}$ and $\mathring{\boldsymbol{C}}_{j,0}^{(m)} = \mathring{\boldsymbol{C}}_{j}^{(m)}$, and then apply Theorem 2 with subscript $t \neq 0$ to the FIMs with dynamic RIS at different observation intervals. $\boxtimes$

To explain the difference between a dynamic RIS and a virtual synthetic RIS in terms of the FIM, we introduce the following notations:

$$\mathring{\boldsymbol{J}}_{j,t}^{\mathcal{A}} = \sum_{m,m' \in \mathcal{A}} \mathring{\boldsymbol{J}}_{j,t}^{(m,m')}, \qquad \text{for } \mathcal{A} \subset \mathcal{N}_{s}^{\text{Dyn}}$$

$$\tilde{\boldsymbol{J}}_{j}^{\mathcal{C}} = \sum_{n \in \mathcal{N}_{t}} \mathring{\boldsymbol{J}}_{j,t_n}^{\mathring{\mathcal{C}}_{t_n}}, \qquad \text{for } \mathcal{C} = \{\mathring{\mathcal{C}}_{t_n} : n \in \mathcal{N}_{t}\}$$

$$\mathring{\boldsymbol{C}}_{j,t}^{\mathcal{A},\mathcal{B}} = \kappa \Big(\sum_{\substack{m \in \mathcal{A} \\ m' \in \mathcal{B}}} \mathring{\boldsymbol{J}}_{j,t}^{(m,m')} \Big), \quad \text{for disjoint } \mathcal{A}, \mathcal{B} \in \sigma\big(\mathcal{N}_{s}^{\text{Syn}}\big)$$

where the set $\mathcal{N}_{s}^{\text{Dyn}}$ of dynamic RIS elements is given by $\mathcal{N}_{s}^{\text{Dyn}} = \bigcup_{n \in \mathcal{N}_{t}} \mathring{\mathcal{N}}_{s,t_n}$, the collection $\mathcal{N}_{s}^{\text{Syn}}$ of the set $\mathring{\mathcal{N}}_{s,t_n}$ of RIS elements for synthesis is given by $\mathcal{N}_{s}^{\text{Syn}} = \{\mathring{\mathcal{N}}_{s,t_n} : n \in \mathcal{N}_{t}\}$, and the σ-field $\sigma(\mathcal{N}_{s}^{\text{Syn}})$ is generated by the collection $\mathcal{N}_{s}^{\text{Syn}}$. For clarity, we consider the case where only sets $\mathring{\mathcal{N}}_{s,t_n}$ of dynamic RIS elements from the adjacent observation intervals have intersections within the collection $\mathcal{N}_{s}^{\text{Syn}}$. In this case, the difference in FIMs between the cases with the dynamic RIS whose elements are indexed by $\mathcal{N}_{s}^{\text{Dyn}}$ and with the synthetic RIS denoted by $\mathcal{N}_{s}^{\text{Syn}}$ is summarized in Proposition 1.

Proposition 1: Consider that the overlapping of dynamic RISs elements for synthesis occurs exclusively between two consecutive observations, and suppose that the velocity of the dynamic non-rotating RIS represented by $\mathring{\mathcal{N}}_{s,t_n}$ for synthesis remains consistent across different observation intervals, aligning with that of the dynamic non-rotating RIS denoted as $\mathcal{N}_{s}^{\text{Dyn}}$. The information difference $\boldsymbol{\Delta}_j(\boldsymbol{p})$ contributed by the scattering path via the RIS between the case with the dynamic RIS represented by $\mathcal{N}_{s}^{\text{Dyn}}$ and with the synthetic RIS represented by $\mathcal{N}_{s}^{\text{Syn}}$ is given by

$$\boldsymbol{\Delta}_j(\boldsymbol{p}) = \tilde{\boldsymbol{J}}_{j}^{\mathcal{N}_{s}^{\text{Syn}}}(\boldsymbol{p}) - \mathring{\boldsymbol{J}}_{j,t}^{\mathcal{N}_{s}^{\text{Dyn}}}(\boldsymbol{p}) \tag{30}$$

$$= \sum_{n=1}^{N_t-1} \mathring{\boldsymbol{J}}_{j}^{\mathcal{V}_n}(\boldsymbol{p}) - \sum_{n=1}^{N_t-1} \sum_{n' \in \mathcal{N}_t \backslash \{n-1,n\}} \mathring{\boldsymbol{C}}_{j}^{\mathcal{V}_n, \tilde{\mathcal{N}}_{s,t_{n'}}}(\boldsymbol{p})$$

$$- \sum_{n=1}^{N_t-1} \sum_{n'=n+1}^{N_t} \mathring{\boldsymbol{C}}_{j}^{\tilde{\mathcal{N}}_{s,t_n}, \tilde{\mathcal{N}}_{s,t_{n'}}}(\boldsymbol{p}) \tag{31}$$

where $\mathcal{V}_n = \mathring{\mathcal{N}}_{s,t_n} \cap \mathring{\mathcal{N}}_{s,t_{n+1}}$ and $\tilde{\mathcal{N}}_{s,t_n} = \mathring{\mathcal{N}}_{s,t_n} \backslash \cup_{i \in \{n-1,n\}} \mathcal{V}_i$. Specially, if $\mathcal{V}_n = \varnothing$, $\forall n \in \mathcal{N}_t$, the information difference

$$\boldsymbol{\Delta}_j(\boldsymbol{p}) = - \sum_{n=1}^{N_t-1} \sum_{n'=n+1}^{N_t} \mathring{\boldsymbol{C}}_{j}^{\mathring{\mathcal{N}}_{s,t_n}, \mathring{\mathcal{N}}_{s,t_{n'}}}(\boldsymbol{p}). \tag{32}$$

Proof: See Appendix C. $\boxtimes$

Corollary 5 (Information difference between the case with dynamic and synthetic RISs in CD scenarios): If all signal components via different paths are completely decoupled, then the information difference of the agent contributed by the j-th anchor between the dynamic and synthetic RISs $\mathcal{N}_{s}^{\text{Dyn}}$ and $\mathcal{N}_{s}^{\text{Syn}}$ is given by $\boldsymbol{\Delta}_j(\boldsymbol{p}) = \sum_{n=1}^{N_t-1} \mathring{\boldsymbol{J}}_{j}^{\mathcal{V}_n}(\boldsymbol{p})$. Specially, if $\mathcal{V}_n = \varnothing$, $\forall n \in \mathcal{N}_t$, it holds that $\boldsymbol{\Delta}_j(\boldsymbol{p}) = \boldsymbol{0}_{3 \times 3}$.

Proof: Apply (20) and (21) to Proposition 1. $\boxtimes$

To maintain simplicity in form, we introduce additional empty sets $\mathring{\mathcal{N}}_{s,N_t+1} = \varnothing$ and $\mathcal{V}_{N_t} = \varnothing$. We emphasize that the same elements in the sequence of set $\mathring{\mathcal{N}}_{s,t_n}$, $\forall n \in \mathcal{N}_t$ correspond to RIS elements at same positions. Since the considered dynamic RIS $\mathring{\mathcal{N}}_j^{\text{Dyn}}$ has the same velocity state as the dynamic small RIS $\mathring{\mathcal{N}}_{s,t_n}$, $n \in \mathcal{N}_t$ for synthesis, the virtual synthetic RIS can be equivalently viewed as a series of dynamic small RISs concatenated together.

If the overlaps among the dynamic small RISs $\mathring{\mathcal{N}}_{s,t_n}$ of different observation intervals are not empty, then for the case where only the adjacent dynamic small RISs have overlaps, Proposition 1 shows that the signals scattered by the synthetic RIS gain information from the signals scattered by the overlaps while lose the information from the couplings of signals scattered by some disjoint regions, such as $\mathcal{V}_n$ and $\mathring{\mathcal{N}}_{s,t_{n'}}$, $n' \in \mathcal{N}_t \backslash \{n-1,n\}$.

If there are no overlaps among the dynamic small RIS $\mathring{\mathcal{N}}_{s,t_n}$ of different observation intervals, then Proposition 1 shows that the signals scattered by the synthetic RIS only lose the information from the couplings of signals scattered by the dynamic small RIS during different observation intervals. Furthermore, consider the case where the dynamic small RIS adopts the setting from the CC scenario. In such scenario, the information from the signal scattered by the synthetic RIS is equivalent to that from the signal scattered by the dynamic large RIS $\mathring{\mathcal{N}}_{s}^{\text{Dyn}}$ with a specific configuration. In particular, this dynamic large RIS controls the signals scattered within the same regions $\mathring{\mathcal{N}}_{s,t_n}$ to be completely coupled. Meanwhile, it ensures that the signals scattered by different regions, specifically $\mathring{\mathcal{N}}_{s,t_n}$ and $\mathring{\mathcal{N}}_{s,t_{n'}}$ where $n \neq n'$, are completely decoupled. In addition, for the case where the dynamic small RIS adopts the setting in the CD scenario, there is no difference between information from the signal scattered by the synthetic RIS and that from the signal scattered by the dynamic large RIS $\mathcal{N}_{s}^{\text{Dyn}}$.

IV. CASE STUDIES

In this section, we illustrate applications of our analysis with several case studies. Although the analysis is valid for any number of anchors and transmitted signals with any bandwidth, we consider simple settings to gain insights.

A. Scenarios and Settings

The considered localization system has one wideband RIS, one agent, and one or two anchors. We set the center frequency and bandwidth of the transmitted signals as 2.4 GHz and 10 MHz, respectively [52]. The observation time T_{obs} is set as 66.67 μs [46]. The transmitted power at the anchors is set to be 1 mW [46]. The dimension l_e of RIS elements is $\lambda_c/4$ [53]. The RIS is rectangular in shape, with its shortest edges parallel to the y-axis. The antennas at the agent and the anchors are small dipole antennas [54] oriented along the y-axis. The operator $\mathcal{P}_{\text{RIS}(m)}$ satisfies

$$\mathcal{P}_{\text{RIS}(m)}\boldsymbol{x} = \tilde{\boldsymbol{p}}^{(m)} \otimes \big[\tilde{\boldsymbol{p}}^{(m)} \otimes \big(\tilde{\boldsymbol{n}}_{\text{RIS}} \otimes (\tilde{\boldsymbol{p}}_j^{(m)} \otimes \boldsymbol{x}) \big) \big], \forall \boldsymbol{x} \in \mathbb{R}^3$$

where the vector $\tilde{\boldsymbol{n}}_{\text{RIS}}$ is the normal vector of the RIS, the vector $\tilde{\boldsymbol{p}}^{(m)} = (\boldsymbol{p} - \boldsymbol{p}^{(m)})/\|\boldsymbol{p} - \boldsymbol{p}^{(m)}\|$, and the vector $\tilde{\boldsymbol{p}}_j^{(m)} = (\boldsymbol{p}^{(m)} - \boldsymbol{p}_j)/\|\boldsymbol{p}^{(m)} - \boldsymbol{p}_j\|$ [29]. The noise figure and
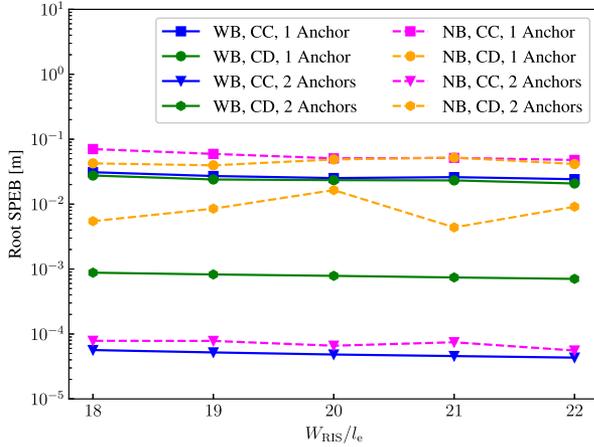
Fig. 3. Comparison of root SPEBs between the holographic localization system with the proposed wideband model and the conventional multi-narrowband model with respect to $W_{\mathrm{RIS}}/l_{\mathrm{e}}$. WB and NB refer to wideband and multi-narrowband, respectively.

Fig. 4. Comparison of root SPEBs with respect to $W_{\mathrm{RIS}}/l_{\mathrm{e}}$ between localization with the static RIS and the dynamic RIS under CC/CD scenarios.

temperature are set as 5 dB and 300 K, respectively [46]. The path loss exponents of the direct path and the reflection and incidence paths via the RIS elements are set as $\mu^{\mathrm{DP}} = 3.5$, $\mu^{\mathrm{SP}} = 2.8$, and $\mu^{\mathrm{IP}} = 2.2$ [55]. Here, μ^{DP} and μ^{SP} affect the attenuations according to (33), (34), and (38), and μ^{IP} affect the attenuation $\alpha_j^{\mathrm{IP}(m)}$ and its time-varying version according to $\alpha_j^{\mathrm{IP}(m)} = \|\boldsymbol{p}^{(m)} - \boldsymbol{p}_j\|^{-\mu^{\mathrm{IP}}/2}$. The spectrum of the baseband signal is an isosceles triangle. The speed of dynamic RISs is set to 5 m/s. In the following, the unit of the coordinates is meter, and 20 realizations of agent positions are used to determine the root SPEB.

B. Performance Evaluation With Wideband and Multi-Narrowband Models

In this simulation, the geometry setting for localization with a static RIS is as follows. The $W_{\mathrm{RIS}} \times W_{\mathrm{RIS}}$ square RIS is centered at $(0, 5, 0)$ and set in xy-plane, and its surface normal is the unit vector of the positive z-axis. The anchor positions $\boldsymbol{p}_1$ and $\boldsymbol{p}_2$ are $(0, 0, 10)$ and $(-5, 0, 5)$, respectively. The agent $\boldsymbol{p}$ is in a $1 \times 1 \times 1$ m^3 space centered at $(5, 0, 5)$. The considered multi-narrowband model implies that the phase responses of RIS elements are piecewise-constant, and the constant phase shift in each narrow band takes the phase response function evaluated at the midpoint frequency of the narrow band. The number of narrow frequency bands is set to 3. The wideband model implies that the phase responses of RIS elements are first-order polynomials. The squared root $W_{\mathrm{RIS}}/l_{\mathrm{e}}$ of the RIS element number varies from 18 to 22.

Fig. 3 shows that the root SPEBs of holographic localization using the multi-narrowband model, where each RIS element requires 3 DOFs, are higher than those using the proposed wideband model, where the phase response functions are first-order polynomials and each RIS element requires only 2 DOFs. This is because the phase spectra of wideband signal components are first-order polynomials with respect to frequency f, allowing the RIS described with the wideband model to manipulate the phase more effectively compared to the multi-narrowband
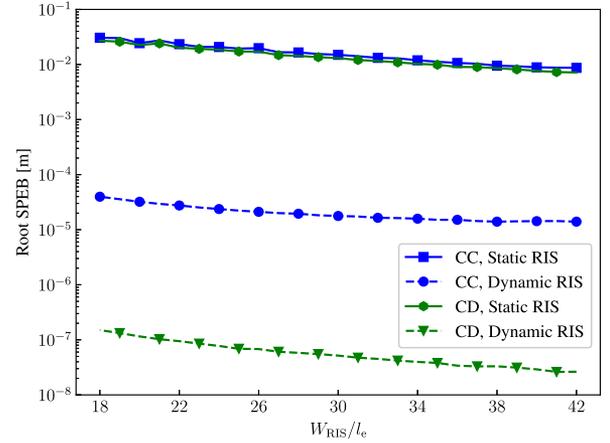
model. Therefore, without the narrowband or multi-narrowband constraints, the potential of wideband RISs can be further enhanced with RIS elements having even fewer DOFs. Fig. 3 also shows that holographic localization with two anchors providing measurement from separated directions achieve lower SPEBs than that with a single anchor, and the CC scenarios outperform the CD. This is because, compared with the single-anchor case, the additional anchor in the two-anchor setup provides position information from another separated direction, thereby enhancing the benefits of increased information intensity in CC scenarios more than the benefits brought by the increased number of information directions in the CD scenarios.

C. Performance Comparison Between Localization With Static RISs and Dynamic RISs

In this comparison, the geometry setting for localization with an RIS is as follows. The $W_{\mathrm{RIS}} \times W_{\mathrm{RIS}}$ square RIS is centered at $(0, 5, 0)$ and set in xy-plane, and its surface normal is the unit vector of the positive z-axis. For the dynamic RIS, the velocity $\mathring{\boldsymbol{v}}^{\mathrm{RIS}}$ of RIS is set as $(-5, 0, 0)$ m/s. The anchor position $\boldsymbol{p}_1$ is $(0, 0, 10)$. The agent $\boldsymbol{p}$ is in a $1 \times 1 \times 1$ m^3 space centered at $(5, 0, 5)$. To compare the gain provided by the static and dynamic RISs in different configurations, we evaluate the root SPEBs of the localization system aided by a static or dynamic RIS in the CD and CC scenarios. It is worthy to note that the agent is placed in the near field of RIS, and when $W_{\mathrm{RIS}}/l_{\mathrm{e}} \geqslant 20$, the anchor is also placed in the near field of the RIS.

Fig. 4 shows that as $W_{\mathrm{RIS}}/l_{\mathrm{e}}$ increases, both static and dynamic RISs provide more position information. Furthermore, CD scenarios yield better results compared to CC scenarios. This is because, under the current settings where only one direct path is LOS, the RIS in a CD scenario provides position information from more directions, enhancing localization accuracy. In contrast, the RIS in a CC scenario combines all signal components scattered through it, offering more intense position information from fewer directions, which results in lower localization accuracy compared to CD. Fig. 4 also shows
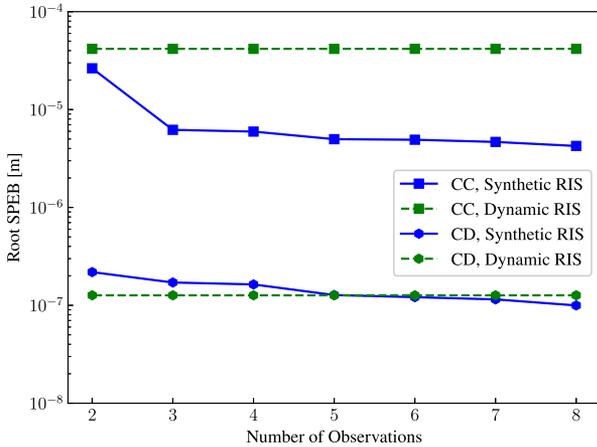
Fig. 5.   Comparison of root SPEB with respect to number of observations for RIS synthesis between localization with a dynamic RIS and a synthetic RIS under CC/CD scenarios.

Fig. 6.   Impact of trajectory perturbation and radius r_{tr} on the root SPEB of a localization system with a synthetic RIS under CC/CD scenarios.

that, with the known RIS velocity, the dynamic RIS significantly improves the root SPEB. This is beacuse the velocity-induced FIM can provide additional angular information, as mentioned in Remark 9.

D. Performance Comparison Between Localization With Dynamic RISs and Synthetic RISs

In the comparison between dynamic RISs and synthetic RISs, we consider a large dynamic RIS of $100l_{\mathrm{e}} \times 20l_{\mathrm{e}}$ and a smaller dynamic RIS of $20l_{\mathrm{e}} \times 20l_{\mathrm{e}}$ for constructing the synthetic RIS. Both RISs move at a velocity of $(5, 0, 0)$ m/s. The center of the large dynamic RIS is at $(0, 5, 0)$. The smaller dynamic surface moves from $(-40l_{\mathrm{e}}, 5, 0)$ to $(40l_{\mathrm{e}}, 5, 0)$, with observations starting at its initial position and ending at its final position, while other observations are evenly distributed between the start and end. The surface normals of RISs are the unit vectors of the positive z-axis. The settings for the agent and anchor are the same as in Section IV-C.

Fig. 5 shows that CD scenarios yield better results compared to CC scenarios, for reasons similar to those illustrated in Fig. 4 of Section IV-C. Specifically, the RIS orientation and the angles between the RIS, the anchor, and the agent remain relatively constant along the synthetic trajectory. Fig. 5 shows that in the CD scenario, the root SPEB decreases as the number of observations increases. This is because the more number of observations, the more RIS elements are synthesized to provide more position information and there is no loss in the FIM provided by the coupling of different signal components, as shown in Corollary 5. Furthermore, Fig. 5 shows that when the number of observations is 5, the large dynamic RIS and the synthetic RIS constructed by the smaller dynamic RISs provide similar position information. This is because when the number of observations is 5, the smaller dynamic RISs at different observation intervals can be exactly concatenated as the large dynamic RIS, and the slight difference comes from the 4 additional observations on the direct path. Therefore, the synthetic RISs can mitigate the multiplicative fading effect without increasing the dimension of RISs or additional PAs.
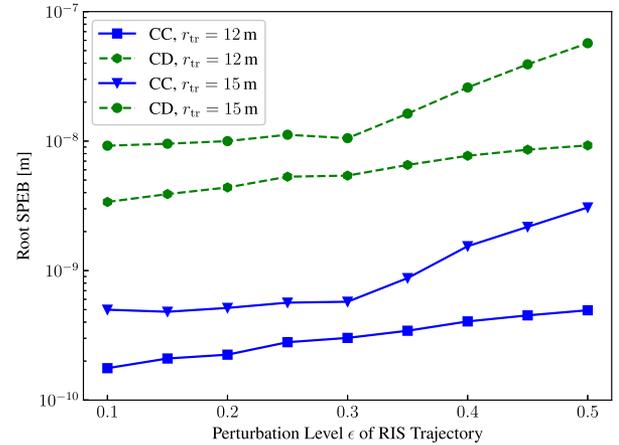
E. Impact of Trajectory for Synthetic RISs on Localization Performance

In the simulation, the RIS velocity is set to be tangent to the trajectory of the RIS in xz-plane. The angular velocity of the RIS is set to keep its normal vector $\tilde{\boldsymbol{n}}_{\mathrm{RIS}}(t)$ in the xz-plane and orthogonal to the RIS velocity $\boldsymbol{v}^{\mathrm{RIS}}(t)$, i.e., $\tilde{\boldsymbol{n}}_{\mathrm{RIS}}(t) = \tilde{\boldsymbol{y}} \otimes \tilde{\boldsymbol{v}}^{\mathrm{RIS}}(t)$, where $\tilde{\boldsymbol{y}}$ and $\tilde{\boldsymbol{v}}^{\mathrm{RIS}}(t)$ are the unit vectors of the y-axis and $\boldsymbol{v}^{\mathrm{RIS}}(t)$, respectively. In addition, without loss of generality, we consider that the RIS moves along the trajectory counter clockwise from top view. The anchor is at $(0, 0, -3.5)$, and the agent is in a $1 \times 1 \times 1$ m³ space centered at $(0, 0, 3.5)$. The trajectory of the dynamic $20l_{\mathrm{e}} \times 20l_{\mathrm{e}}$ RIS is a circle with a radius of r_{tr} centered at $(0, 5, 0)$ in the xz-plane. The number of observations for constructing the synthetic RIS is set to 10. Moreover, to assess the impact of perturbation on trajectories, the perturbed trajectories are generated as follows. Fifty points are uniformly sampled along the circular trajectory. Each point receives a random radial perturbation distributed uniformly in $[-\epsilon r_{\mathrm{tr}}, \epsilon r_{\mathrm{tr}}]$, where ϵ is the perturbation level. A two-hundred-point cubic spline interpolation of these points generates the perturbed trajectory, which determines the velocity directions and orientations of the dynamic RISs in different observation intervals. The perturbation level ϵ varies from 0.1 to 0.5 in the simulations.

Fig. 6 shows that CC scenarios outperform CD scenarios. for the reason similar to those illustrated in Fig. 3 of Section IV-B. Specifically, the synthetic RIS, which encircles the anchor and the agent with a closed trajectory, provides position information from separated directions. Fig. 6 shows that as the trajectory radius r_{tr} decreases, the root SPEBs improve significantly. This is because the lengths of the scattering paths via the dynamic RISs decrease and the signal attenuations are weakened. Fig. 6 also shows that root SPEBs decrease as the perturbation level increases when the perturbation level $\epsilon \geqslant 0.1$. This is because large perturbation on the trajectory can weaken the signal components scattered by the RIS by changing the RIS orientation and decreasing the polarization attenuations $\mathring{\gamma}_{j,t}^{\mathrm{RIS}(m)}$. Therefore, for scenarios involving a synthetic RIS whose trajectory surrounds the anchor and agent, a reduction in both the trajectory radius and the perturbation level can enhance localization accuracy.

V. Conclusion

This paper presented a general signal model for localization systems with a wideband RIS and determined the performance limits of RIS-aided wideband localization. A signal processing framework with synthetic RISs was proposed to enhance the localization accuracy. Results show that with the proposed wideband models, an RIS whose elements have a polynomial phase response with two DOFs can provide more position information with less DOFs than those in piecewise-constant phase response with more DOFs. Besides, a dynamic RIS can provide more position information than a static RIS due to velocity-induced FIMs. Moreover, a small dynamic RIS, through multiple measurements, can be synthesized to outperform a large one. The case studies show that CD scenarios outperform CC in cases with a single or multiple closely-spaced measurement directions provided by an RIS or anchors, such as single-anchor cases involving a static RIS, a dynamic RIS, or a synthetic RIS with a short-segment trajectory. Conversely, CC scenarios outperform CD in cases with multiple separated measurement directions provided by an RIS or anchors, such as the multi-anchor case and the single-anchor case involving a synthetic RIS with a trajectory surrounding the anchor and agent. In addition, reducing the perturbation level and radius of the RIS trajectory surrounding the anchor and agent can enhance the position information brought by the synthetic RIS. The findings in this paper provided guidelines for the design of wideband localization with synthetic RISs.

Appendix A

The channel parameters $\boldsymbol{\eta}$ of the system can be partitioned as $[(\boldsymbol{\eta}_1^{\mathrm{DP}})^{\mathrm{T}} \cdots (\boldsymbol{\eta}_{N_{\mathrm{b}}}^{\mathrm{DP}})^{\mathrm{T}} (\boldsymbol{\eta}^{\mathrm{SP}(1)})^{\mathrm{T}} \cdots (\boldsymbol{\eta}^{\mathrm{SP}(N_{\mathrm{s}})})^{\mathrm{T}}]^{\mathrm{T}}$. The channel parameters $\boldsymbol{\eta}_j^{\mathrm{DP}}$ of the direct path between the j-th anchor and the agent are given by $[\tilde{\tau}_j \quad \psi_j \quad \varphi_j \quad \alpha_j^{\mathrm{DP}}]^{\mathrm{T}}$, where $\tilde{\tau}_j = \|\boldsymbol{p} - \boldsymbol{p}_j\|$, $\psi_j = \arccos(\frac{z - z_j}{\|\boldsymbol{p} - \boldsymbol{p}_j\|})$, $\varphi_j = \arctan2(y - y_j, x - x_j)$, and

$$\alpha_j^{\mathrm{DP}} = \|\boldsymbol{p} - \boldsymbol{p}_j\|^{-\mu^{\mathrm{DP}}/2}. \tag{33}$$

The channel parameters $\boldsymbol{\eta}^{\mathrm{SP}(m)}$ of the reflection path via the m-th static RIS element are given by $[\tilde{\tau}^{\mathrm{SP}(m)} \quad \psi_{\mathrm{A}}^{(m)} \quad \varphi_{\mathrm{A}}^{(m)} \quad \alpha^{\mathrm{SP}(m)}]^{\mathrm{T}}$, where $\tilde{\tau}^{\mathrm{SP}(m)} = \|\boldsymbol{p} - \boldsymbol{p}^{(m)}\|$, $\psi_{\mathrm{A}}^{(m)} = \arccos(\frac{z^{(m)} - z}{\|\boldsymbol{p} - \boldsymbol{p}^{(m)}\|})$, $\varphi_{\mathrm{A}}^{(m)} = \arctan2(y^{(m)} - y, x^{(m)} - x)$, and

$$\alpha^{\mathrm{SP}(m)} = \|\boldsymbol{p} - \boldsymbol{p}^{(m)}\|^{-\mu^{\mathrm{SP}}/2}. \tag{34}$$

Here, μ^{DP} and μ^{SP} are the path loss exponents of the direct path, and the reflection path via the m-th RIS element, respectively. Therefore, the Jacobian matrices $\boldsymbol{Q}_j^{\mathrm{DP}}$ and $\boldsymbol{Q}^{\mathrm{SP}(m)}$ are

$$\boldsymbol{Q}_j^{\mathrm{DP}} = \begin{bmatrix} \boldsymbol{q}_0(\psi_j, \varphi_j)^{\mathrm{T}} \\ \frac{1}{\|\boldsymbol{p} - \boldsymbol{p}_j\|} \boldsymbol{q}_0(\psi_j + \pi/2, \varphi_j)^{\mathrm{T}} \\ \frac{1}{\|\boldsymbol{p} - \boldsymbol{p}_j\| \sin\psi_j} \boldsymbol{q}_0(\pi/2, \varphi_j + \pi/2)^{\mathrm{T}} \\ -\frac{\mu^{\mathrm{DP}}}{2\|\boldsymbol{p} - \boldsymbol{p}_j\|^{1 + \mu^{\mathrm{DP}}/2}} \boldsymbol{q}_0(\psi_j, \varphi_j)^{\mathrm{T}} \end{bmatrix}^{\mathrm{T}} \tag{35}$$

$$\boldsymbol{Q}^{\mathrm{SP}(m)} = \begin{bmatrix} \boldsymbol{q}_0(\psi^{(m)}, \varphi^{(m)})^{\mathrm{T}} \\ \frac{1}{\|\boldsymbol{p} - \boldsymbol{p}^{(m)}\|} \boldsymbol{q}_0(\psi^{(m)} - \pi/2, \varphi^{(m)})^{\mathrm{T}} \\ \frac{1}{\|\boldsymbol{p} - \boldsymbol{p}^{(m)}\| \sin\psi^{(m)}} \boldsymbol{q}_0(\pi/2, \varphi^{(m)} + \pi/2)^{\mathrm{T}} \\ -\frac{\mu^{\mathrm{SP}}}{2\|\boldsymbol{p} - \boldsymbol{p}^{(m)}\|^{1 + \mu^{\mathrm{SP}}/2}} \boldsymbol{q}_0(\psi^{(m)}, \varphi^{(m)})^{\mathrm{T}} \end{bmatrix}^{\mathrm{T}}. \tag{36}$$

Due to the independence among different anchors, the total FIM can be expressed as the sum of FIMs from the measurement between the agent and each anchor, i.e., $\boldsymbol{J}(\boldsymbol{p}) = \sum_{j \in \mathcal{N}_{\mathrm{b}}} \boldsymbol{J}_j(\boldsymbol{p})$. By the definition of FIM in (7), the chain rule of differentiation, the rule of block matrix multiplication, and Lemma 1, it holds that

$$\boldsymbol{J}_j(\boldsymbol{p}) = \boldsymbol{Q}_j^{\mathrm{DP}} \boldsymbol{J}_j(\boldsymbol{\eta}_j^{\mathrm{DP}}) (\boldsymbol{Q}_j^{\mathrm{DP}})^{\mathrm{T}}$$
$$+ \sum_{m, m' \in \mathcal{N}_{\mathrm{s}}} \boldsymbol{Q}^{\mathrm{SP}(m)} \boldsymbol{J}_j(\boldsymbol{\eta}^{\mathrm{SP}(m)}, \boldsymbol{\eta}^{\mathrm{SP}(m')}) (\boldsymbol{Q}^{\mathrm{SP}(m')})^{\mathrm{T}}$$
$$+ \sum_{m \in \mathcal{N}_{\mathrm{s}}} \boldsymbol{Q}^{\mathrm{DP}} \boldsymbol{C}_j(\boldsymbol{\eta}^{\mathrm{DP}}, \boldsymbol{\eta}^{\mathrm{SP}(m)}) (\boldsymbol{Q}^{\mathrm{SP}(m)})^{\mathrm{T}} \tag{37}$$

where $\boldsymbol{\eta}_j = [(\boldsymbol{\eta}_j^{\mathrm{DP}})^{\mathrm{T}} (\boldsymbol{\eta}^{\mathrm{SP}})^{\mathrm{T}}]^{\mathrm{T}}$ with $\boldsymbol{\eta}^{\mathrm{SP}} = [(\boldsymbol{\eta}^{\mathrm{SP}(1)})^{\mathrm{T}} (\boldsymbol{\eta}^{\mathrm{SP}(2)})^{\mathrm{T}} \cdots (\boldsymbol{\eta}^{\mathrm{SP}(N_{\mathrm{s}})})^{\mathrm{T}}]^{\mathrm{T}}$; the FIM $\boldsymbol{J}_j(\boldsymbol{\theta})$ of the parameter vector $\boldsymbol{\theta}$ is defined as in (9), specifically given by $\frac{2}{N_0} \int_{-\infty}^{\infty} \frac{\partial R_j(f)}{\partial \boldsymbol{\theta}} \frac{\partial R_j^*(f)}{\partial \boldsymbol{\theta}^{\mathrm{T}}} df$ with the Fourier transform $R_j(f) = \chi_j R_j^{\mathrm{DP}}(f) + \sum_{m \in \mathcal{N}_{\mathrm{s}}} R_j^{\mathrm{RIS}(m)}(f)$; the FIM $\boldsymbol{J}_j(\boldsymbol{\eta}^{\mathrm{SP}(m)}, \boldsymbol{\eta}^{\mathrm{SP}(m')})$ and $\boldsymbol{C}(\boldsymbol{\eta}^{\mathrm{DP}}, \boldsymbol{\eta}^{\mathrm{SP}(m)})$ are respectively given by $\frac{2}{N_0} \int_{-\infty}^{\infty} \frac{\partial R_j(f)}{\partial \boldsymbol{\eta}^{\mathrm{SP}(m)}} \frac{\partial R_j^*(f)}{\partial (\boldsymbol{\eta}^{\mathrm{SP}(m')})^{\mathrm{T}}} df$ and $\frac{2}{N_0} \kappa(\int_{-\infty}^{\infty} \frac{\partial R_j(f)}{\partial \boldsymbol{\eta}^{\mathrm{DP}}} \frac{\partial R_j^*(f)}{\partial (\boldsymbol{\eta}^{\mathrm{SP}(m)})^{\mathrm{T}}} df)$.

By the linearity of the Fourier transform and the fact that $\chi_j^2 = \chi_j$, the indicator χ_j of the LOS path can be extracted from the related FIM. Define

$$\boldsymbol{J}_j^{\mathrm{DP}}(\boldsymbol{p}) = \boldsymbol{Q}_j^{\mathrm{DP}} \boldsymbol{J}_j(\boldsymbol{\eta}_j^{\mathrm{DP}})\big|_{\chi_j = 1} (\boldsymbol{Q}_j^{\mathrm{DP}})^{\mathrm{T}}$$
$$\boldsymbol{J}_j^{(m, m')}(\boldsymbol{p}) = \boldsymbol{Q}^{\mathrm{SP}(m)} \boldsymbol{J}_j(\boldsymbol{\eta}^{\mathrm{SP}(m)}, \boldsymbol{\eta}^{\mathrm{SP}(m')}) (\boldsymbol{Q}^{\mathrm{SP}(m')})^{\mathrm{T}}$$
$$\boldsymbol{C}_j^{(m)}(\boldsymbol{p}) = \boldsymbol{Q}^{\mathrm{DP}} \boldsymbol{C}_j(\boldsymbol{\eta}^{\mathrm{DP}}, \boldsymbol{\eta}^{\mathrm{SP}(m)})\big|_{\chi_j = 1} (\boldsymbol{Q}^{\mathrm{SP}(m)})^{\mathrm{T}}$$

and substitute them into (37), and then (14) is proven. By Definitions 3–5, (15)–(17) can be proved after some algebra.

Appendix B

For any observation interval $[t, t + T_{\mathrm{obs}})$, the channel parameters $\mathring{\boldsymbol{\eta}}_t^{\mathrm{SP}(m)}$ of the path between the dynamic m-th RIS element and the agent are given by $[\mathring{\tilde{\tau}}_t^{\mathrm{SP}(m)} \quad \mathring{\psi}_{\mathrm{A},t}^{(m)} \quad \mathring{\varphi}_{\mathrm{A},t}^{(m)} \quad \mathring{\alpha}_t^{\mathrm{SP}(m)} \quad \mathring{\nu}_t^{\mathrm{SP}(m)}]^{\mathrm{T}}$, where $\mathring{\tilde{\tau}}_t^{\mathrm{SP}(m)} = \|\mathring{\boldsymbol{p}}_t^{(m)} - \boldsymbol{p}\|$, $\mathring{\psi}_{\mathrm{A},t}^{(m)} = \arccos(\frac{\mathring{z}_t^{(m)} - z}{\|\boldsymbol{p} - \mathring{\boldsymbol{p}}_t^{(m)}\|})$, $\mathring{\varphi}_{\mathrm{A},t}^{(m)} = \arctan2(\mathring{y}_t^{(m)} - y, \mathring{x}_t^{(m)} - x)$, $\mathring{\nu}_t^{\mathrm{SP}(m)} = \frac{1}{c} \langle \mathring{\boldsymbol{v}}_t^{(m)}, \boldsymbol{q}_0(\mathring{\psi}_t^{(m)}, \mathring{\varphi}_t^{(m)}) \rangle$, and

$$\mathring{\alpha}_t^{\mathrm{SP}(m)} = \|\boldsymbol{p} - \mathring{\boldsymbol{p}}_t^{(m)}\|^{-\mu^{\mathrm{SP}}/2}. \tag{38}$$

The Jacobian matrix $\mathring{\boldsymbol{Q}}_t^{\mathrm{SP}(m)}$ can be partitioned by the Doppler-shifted matrix $\mathring{\boldsymbol{Q}}_t^{\mathrm{D}(m)}$ and the velocity-induced vector $\mathring{\boldsymbol{q}}_t^{\mathrm{V}(m)}$,

given by

$$\mathring{\boldsymbol{Q}}_t^{\mathrm{SP}(m)} = \frac{\partial (\mathring{\boldsymbol{\eta}}_t^{\mathrm{SP}(m)})^{\mathrm{T}}}{\partial \boldsymbol{p}} = \begin{bmatrix} \mathring{\boldsymbol{Q}}_t^{\mathrm{D}(m)} & \mathring{\boldsymbol{q}}_t^{\mathrm{V}(m)} \end{bmatrix}. \tag{39}$$

By the definitions of the channel parameters $\mathring{\boldsymbol{\eta}}_t^{\mathrm{SP}(m)}$, $\mathring{\boldsymbol{Q}}_t^{\mathrm{D}(m)}$ and $\mathring{\boldsymbol{q}}_t^{\mathrm{V}(m)}$ are specifically given by

$$\mathring{\boldsymbol{Q}}_t^{\mathrm{D}(m)} = \begin{bmatrix} \boldsymbol{q}_0(\mathring{\psi}_t^{(m)}, \mathring{\varphi}_t^{(m)})^{\mathrm{T}} \\ \frac{\boldsymbol{q}_0(\mathring{\psi}_t^{(m)} - \pi/2, \mathring{\varphi}_t^{(m)})^{\mathrm{T}}}{\|\boldsymbol{p} - \mathring{\boldsymbol{p}}_t^{(m)}\|} \\ \frac{\boldsymbol{q}_0(\pi/2, \mathring{\varphi}_t^{(m)} + \pi/2)^{\mathrm{T}}}{\|\boldsymbol{p} - \mathring{\boldsymbol{p}}_t^{(m)}\| \sin \mathring{\psi}_t^{(m)}} \\ \frac{-\mu^{\mathrm{SP}} \boldsymbol{q}_0(\mathring{\psi}_t^{(m)}, \mathring{\varphi}_t^{(m)})^{\mathrm{T}}}{2\|\boldsymbol{p} - \mathring{\boldsymbol{p}}_t^{(m)}\|^{1+\mu^{\mathrm{SP}}/2}} \end{bmatrix}^{\mathrm{T}} \tag{40}$$

$$\mathring{\boldsymbol{q}}_t^{\mathrm{V}(m)} = \frac{(\mathring{\boldsymbol{v}}_t^{(m)})^{\mathrm{T}}}{c\|\boldsymbol{p} - \mathring{\boldsymbol{p}}_t^{(m)}\|}$$
$$\times \left[\boldsymbol{I}_3 - \boldsymbol{q}_0(\mathring{\psi}_t^{(m)}, \mathring{\varphi}_t^{(m)}) \boldsymbol{q}_0(\mathring{\psi}_t^{(m)}, \mathring{\varphi}_t^{(m)})^{\mathrm{T}} \right]. \tag{41}$$

Define

$$\boldsymbol{J}_j^{\mathrm{DP}}(\boldsymbol{p}) = \boldsymbol{Q}_j^{\mathrm{DP}} \mathring{\boldsymbol{J}}_j(\boldsymbol{\eta}_j^{\mathrm{DP}}) \big|_{\mathring{\chi}_{j,t}=1} (\boldsymbol{Q}_j^{\mathrm{DP}})^{\mathrm{T}}$$

$$\mathring{\boldsymbol{J}}_{j,t}^{(m,m')}(\boldsymbol{p}) = \mathring{\boldsymbol{Q}}_t^{\mathrm{SP}(m)} \mathring{\boldsymbol{J}}_{j,t}(\mathring{\boldsymbol{\eta}}_t^{\mathrm{SP}(m)}, \mathring{\boldsymbol{\eta}}_t^{\mathrm{SP}(m')}) (\mathring{\boldsymbol{Q}}_t^{\mathrm{SP}(m)})^{\mathrm{T}} \tag{42}$$

$$\mathring{\boldsymbol{C}}_{j,t}^{(m)}(\boldsymbol{p}) = \boldsymbol{Q}^{\mathrm{DP}} \mathring{\boldsymbol{C}}_{j,t}(\boldsymbol{\eta}^{\mathrm{DP}}, \mathring{\boldsymbol{\eta}}_{j,t}^{\mathrm{SP}(m)}) \big|_{\mathring{\chi}_{j,t}=1} (\mathring{\boldsymbol{Q}}_t^{\mathrm{SP}(m)})^{\mathrm{T}} \tag{43}$$

where the FIM $\mathring{\boldsymbol{J}}_j(\boldsymbol{\theta})$ of the parameter vector $\boldsymbol{\theta}$ is $\frac{2}{N_0}$ $\int_{-\infty}^{\infty} \frac{\partial \mathring{R}_{j,t}(f)}{\partial \boldsymbol{\theta}} \frac{\partial \mathring{R}_{j,t}^*(f)}{\partial \boldsymbol{\theta}^{\mathrm{T}}} df$ with the Fourier transform $\mathring{R}_{j,t}(f) = \mathring{\chi}_{j,t} R_j^{\mathrm{DP}}(f) + \sum_{m \in \mathring{N}_{\mathrm{s},t}} \mathring{R}_{j,t}^{\mathrm{RIS}(m)}(f)$; the FIM $\mathring{\boldsymbol{J}}_j(\mathring{\boldsymbol{\eta}}_{j,t}^{\mathrm{SP}(m)}, \mathring{\boldsymbol{\eta}}_{j,t}^{\mathrm{SP}(m')})$ is $\frac{2}{N_0} \int_{-\infty}^{\infty} \frac{\partial \mathring{R}_{j,t}(f)}{\partial \mathring{\boldsymbol{\eta}}_{j,t}^{\mathrm{SP}(m)}} \frac{\partial \mathring{R}_{j,t}^*(f)}{\partial (\mathring{\boldsymbol{\eta}}_{j,t}^{\mathrm{SP}(m')})^{\mathrm{T}}} df$; and the FIM $\mathring{\boldsymbol{C}}_{j,t}(\boldsymbol{\eta}^{\mathrm{DP}}, \mathring{\boldsymbol{\eta}}_{j,t}^{\mathrm{SP}(m)})$ is $\frac{2}{N_0} \kappa(\int_{-\infty}^{\infty} \frac{\partial \mathring{R}_{j,t}(f)}{\partial \boldsymbol{\eta}^{\mathrm{DP}}} \frac{\partial \mathring{R}_{j,t}^*(f)}{\partial (\mathring{\boldsymbol{\eta}}_{j,t}^{\mathrm{SP}(m)})^{\mathrm{T}}} df)$. Then, (22) can be proved similar to the proof of (14).

Define the Doppler-shifted and velocity-induced components $\mathring{\boldsymbol{J}}_{j,t}^{\mathrm{D}(m,m')}(\boldsymbol{p})$ and $\mathring{\boldsymbol{J}}_{j,t}^{\mathrm{V}(m,m')}(\boldsymbol{p})$ respectively as $\mathring{\boldsymbol{Q}}_t^{\mathrm{D}(m)} [\mathring{\boldsymbol{J}}_{j,t}(\mathring{\boldsymbol{\eta}}_t^{\mathrm{SP}(m)}, \mathring{\boldsymbol{\eta}}_t^{\mathrm{SP}(m')})]_{1:4,1:4} (\mathring{\boldsymbol{Q}}_t^{\mathrm{D}(m')})^{\mathrm{T}}$ and $\kappa(\mathring{\boldsymbol{Q}}_t^{\mathrm{D}(m)} [\mathring{\boldsymbol{J}}_{j,t}(\mathring{\boldsymbol{\eta}}_t^{\mathrm{SP}(m)}, \mathring{\boldsymbol{\eta}}_t^{\mathrm{SP}(m')})]_{1:4,5} (\mathring{\boldsymbol{q}}_t^{\mathrm{V}(m')})^{\mathrm{T}}) + [\mathring{\boldsymbol{J}}_{j,t}(\mathring{\boldsymbol{\eta}}_t^{\mathrm{SP}(m)}, \mathring{\boldsymbol{\eta}}_t^{\mathrm{SP}(m')})]_{5,5} \mathring{\boldsymbol{q}}_t^{\mathrm{V}(m)} (\mathring{\boldsymbol{q}}_t^{\mathrm{V}(m')})^{\mathrm{T}}$. Substitute (39) into (42), and then (23) holds due to the rule of block matrix multiplication. In addition, with Definitions 3, 7–10 and $t = 0$, (24) and (25) are proved.

Similarly, define the Doppler-shifted and velocity-induced components $\mathring{\boldsymbol{C}}_{j,t}^{\mathrm{D}(m)}(\boldsymbol{p})$ and $\mathring{\boldsymbol{C}}_{j,t}^{\mathrm{V}(m)}(\boldsymbol{p})$ respectively as

$$\mathring{\boldsymbol{C}}_{j,t}^{\mathrm{D}(m)}(\boldsymbol{p}) = \boldsymbol{Q}^{\mathrm{DP}} [\mathring{\boldsymbol{C}}_{j,t}(\boldsymbol{\eta}^{\mathrm{DP}}, \mathring{\boldsymbol{\eta}}_{j,t}^{\mathrm{SP}(m)})]_{1:4,1:4} \big|_{\mathring{\chi}_{j,t}=1} (\mathring{\boldsymbol{Q}}_t^{\mathrm{D}(m)})^{\mathrm{T}}$$

$$\mathring{\boldsymbol{C}}_{j,t}^{\mathrm{V}(m)}(\boldsymbol{p}) = \boldsymbol{Q}^{\mathrm{DP}} [\mathring{\boldsymbol{C}}_{j,t}(\boldsymbol{\eta}^{\mathrm{DP}}, \mathring{\boldsymbol{\eta}}_{j,t}^{\mathrm{SP}(m)})]_{1:4,5} \big|_{\mathring{\chi}_{j,t}=1} (\mathring{\boldsymbol{q}}_t^{\mathrm{V}(m)})^{\mathrm{T}}.$$

Substitute (39) into (43), and then (26) holds due to the rule of block matrix multiplication. In addition, with Definitions 3, 7, 9, 10 and $t = 0$, (27) and (28) are proved.

APPENDIX C

By the definitions of $\mathcal{V}_n$ and $\tilde{\mathcal{N}}_{\mathrm{s},t_n}$, set $\mathring{\mathcal{N}}_{\mathrm{s},t_n}$ can be expressed as the union of disjoint sets. Specifically, it holds that $\mathring{\mathcal{N}}_{\mathrm{s},t_n} = \mathcal{V}_{n-1} \cup \tilde{\mathcal{N}}_{\mathrm{s},t_n} \cup \mathcal{V}_n$, $\forall n \in \mathcal{N}_{\mathrm{t}}$, where $\mathcal{V}_0 = \mathcal{V}_{N_{\mathrm{t}}} = \varnothing$. Furthermore, the set $\mathcal{N}_{\mathrm{s}}^{\mathrm{Dyn}}$ can also be expressed as the union of disjoint sets. Specifically, it holds that $\mathcal{N}_{\mathrm{s}}^{\mathrm{Dyn}} = (\cup_{n \in \mathcal{N}_{\mathrm{t}}} \mathcal{V}_n) \cup (\cup_{n \in \mathcal{N}_{\mathrm{t}}} \tilde{\mathcal{N}}_{\mathrm{s},t_n})$. For a sequence of disjoint sets $\mathcal{A}_i$, $i \in \mathcal{I}$, where $\mathcal{I}$ is the index set, we have

$$\mathring{\boldsymbol{J}}_{j,t}^{\cup_i \mathcal{A}_i}(\boldsymbol{p}) = \sum_{i \in \mathcal{I}} \mathring{\boldsymbol{J}}_{j,t}^{\mathcal{A}_i}(\boldsymbol{p}) + \sum_{\substack{i,i' \in \mathcal{I} \\ i < i'}} \boldsymbol{C}_{j,t}^{\mathcal{A}_i, \mathcal{A}_{i'}}(\boldsymbol{p}). \tag{44}$$

With (44), the FIM contributed by the scattering paths via the synthetic RIS can be expressed as

$$\tilde{\boldsymbol{J}}_j^{\mathcal{N}_{\mathrm{s}}^{\mathrm{Syn}}}(\boldsymbol{p}) = \sum_{n=1}^{N_{\mathrm{t}}} \left[\mathring{\boldsymbol{J}}_{j,t_n}^{\mathcal{V}_{n-1}}(\boldsymbol{p}) + \mathring{\boldsymbol{J}}_{j,t_n}^{\mathcal{V}_n}(\boldsymbol{p}) + \mathring{\boldsymbol{J}}_{j,t_n}^{\tilde{\mathcal{N}}_{\mathrm{s},t_n}}(\boldsymbol{p}) \right]$$
$$+ \sum_{n=1}^{N_{\mathrm{t}}} \left[\mathring{\boldsymbol{C}}_{j,t_n}^{\mathcal{V}_{n-1}, \tilde{\mathcal{N}}_{\mathrm{s},t_n}}(\boldsymbol{p}) + \mathring{\boldsymbol{C}}_{j,t_n}^{\mathcal{V}_{n-1}, \tilde{\mathcal{N}}_{\mathrm{s},t_n}}(\boldsymbol{p}) \right] \tag{45}$$

and the FIM contributed by the scattering path via the dynamic RIS can be expressed as

$$\mathring{\boldsymbol{J}}_{j,t}^{\mathcal{N}_{\mathrm{s}}^{\mathrm{Dyn}}}(\boldsymbol{p}) = \sum_{n \in \mathcal{N}_{\mathrm{t}}} \mathring{\boldsymbol{J}}_{j,t}^{\mathcal{V}_n}(\boldsymbol{p}) + \sum_{n \in \mathcal{N}_{\mathrm{t}}} \mathring{\boldsymbol{J}}_{j,t}^{\tilde{\mathcal{N}}_{\mathrm{s},t_n}}(\boldsymbol{p})$$
$$+ \sum_{\substack{n,n' \in \mathcal{N}_{\mathrm{t}} \\ n' > n}} \left[\mathring{\boldsymbol{C}}_{j,t}^{\mathcal{V}_n, \mathcal{V}_{n'}} + \mathring{\boldsymbol{C}}_{j,t}^{\tilde{\mathcal{N}}_{\mathrm{s},t_n}, \tilde{\mathcal{N}}_{\mathrm{s},t_{n'}}}(\boldsymbol{p}) \right]$$
$$+ \sum_{n,n' \in \mathcal{N}_{\mathrm{t}}} \mathring{\boldsymbol{C}}_{j,t}^{\mathcal{V}_n, \tilde{\mathcal{N}}_{\mathrm{s},t_{n'}}}(\boldsymbol{p}). \tag{46}$$

Since the velocity of the dynamic RIS represented by $\mathring{\mathcal{N}}_{\mathrm{s},t_n}$ for synthesis remains consistent across different observation intervals, aligning with that of the dynamic RIS denoted as $\mathcal{N}_{\mathrm{s}}^{\mathrm{Dyn}}$, for all $m, m' \in \mathcal{N}_{\mathrm{s}}^{\mathrm{Dyn}}$, it holds that $\mathring{\boldsymbol{J}}_{j,t}^{(m,m')}(\boldsymbol{p}) = \mathring{\boldsymbol{J}}_{j,t_n}^{(m,m')}(\boldsymbol{p})$, $\forall n \in \mathcal{N}_{\mathrm{t}}$. Furthermore, by substituting (45) and (46) into (30), the (31) is proved. In addition, for the case where $\mathcal{V}_n = \varnothing$, $n \in \mathcal{N}_{\mathrm{t}}$, the first two terms in (31) are zero matrices, so (32) is proved.

ACKNOWLEDGMENT

REFERENCES

[1] M. Z. Win, Z. Wang, Z. Liu, Y. Shen, and A. Conti, "Location awareness via intelligent surfaces: A path toward holographic NLN," *IEEE Veh. Technol. Mag.*, vol. 17, no. 2, pp. 37–45, Jun. 2022.

[2] G. Pasolini et al., "Smart city pilot projects using LoRa and IEEE 802.15.4 technologies," *Sensors*, vol. 18, no. 4, Apr. 2018, Art. no. 1118.

[3] G. Torsoli, M. Z. Win, and A. Conti, "Blockage intelligence in complex environments for beyond 5G localization," *IEEE J. Sel. Areas Commun.*, vol. 41, no. 6, pp. 1688–1701, Jun. 2023.

[4] F. Liu et al., "Integrated sensing and communications: Towards dual-functional wireless networks for 6G and beyond," *IEEE J. Sel. Areas Commun.*, vol. 40, no. 6, pp. 1728–1767, Jun. 2022.

[5] G. Kwon, Z. Liu, A. Conti, H. Park, and M. Z. Win, "Integrated localization and communication for efficient millimeter wave networks," *IEEE J. Sel. Areas Commun.*, vol. 41, no. 12, pp. 3925–3941, Dec. 2023.

[6] L. Wu, K. V. Mishra, M. R. B. Shankar, and B. Ottersten, "Resource allocation in heterogeneously-distributed joint radar-communications under asynchronous Bayesian tracking framework," *IEEE J. Sel. Areas Commun.*, vol. 40, no. 7, pp. 2026–2042, Jul. 2022.

[7] S. H. Dokhanchi, B. S. Mysore, K. V. Mishra, and B. Ottersten, "A mmWave automotive joint radar-communications system," *IEEE Trans. Aerosp. Electron. Syst.*, vol. 55, no. 3, pp. 1241–1260, Jun. 2019.

[8] Z. Liu, A. Conti, S. K. Mitter, and M. Z. Win, "Communication-efficient distributed learning over networks–Part I: Sufficient conditions for accuracy," *IEEE J. Sel. Areas Commun.*, vol. 41, no. 4, pp. 1081–1101, Apr. 2023.

[9] Z. Liu, A. Conti, S. K. Mitter, and M. Z. Win, "Communication-efficient distributed learning over networks–Part II: Necessary conditions for accuracy," *IEEE J. Sel. Areas Commun.*, vol. 41, no. 4, pp. 1102–1119, Apr. 2023.

[10] S. Das and J. M. F. Moura, "Consensus+innovations distributed Kalman filter with optimized gains," *IEEE Trans. Signal Process.*, vol. 65, no. 2, pp. 467–481, Jan. 2017.

[11] S. Kar and J. M. F. Moura, "Consensus + innovations distributed inference over networks: Cooperation and sensing in networked systems," *IEEE Signal Process. Mag.*, vol. 30, no. 3, pp. 99–109, May 2013.

[12] Z. Liu, A. Conti, S. K. Mitter, and M. Z. Win, "Continuous-time distributed filtering with sensing and communication constraints," *IEEE J. Sel. Areas Inf. Theory*, vol. 4, pp. 667–681, 2023.

[13] N. C. Luong, D. T. Hoang, P. Wang, D. Niyato, D. I. Kim, and Z. Han, "Data collection and wireless communication in Internet of Things (IoT) using economic analysis and pricing models: A survey," *IEEE Commun. Surveys Tuts.*, vol. 18, no. 4, pp. 2546–2590, Fourthquarter 2016.

[14] M. Z. Win, F. Meyer, Z. Liu, W. Dai, S. Bartoletti, and A. Conti, "Efficient multi-sensor localization for the Internet of Things: Exploring a new class of scalable localization algorithms," *IEEE Signal Process. Mag.*, vol. 35, no. 5, pp. 153–167, Sep. 2018.

[15] A. Conti, S. Mazuelas, S. Bartoletti, W. C. Lindsey, and M. Z. Win, "Soft information for localization-of-things," *Proc. IEEE*, vol. 107, no. 11, pp. 2240–2264, Nov. 2019.

[16] F. Morselli, S. M. Razavi, M. Z. Win, and A. Conti, "Soft information based localization for 5G networks and beyond," *IEEE Trans. Wireless Commun.*, vol. 22, no. 12, pp. 9923–9938, Dec. 2023.

[17] Q. Wu and R. Zhang, "Intelligent reflecting surface enhanced wireless network via joint active and passive beamforming," *IEEE Trans. Wireless Commun.*, vol. 18, no. 11, pp. 5394–5409, Nov. 2019.

[18] M. D. Renzo et al., "Smart radio environments empowered by reconfigurable intelligent surfaces: How it works, state of research, and the road ahead," *IEEE J. Sel. Areas Commun.*, vol. 38, no. 11, pp. 2450–2525, Nov. 2020.

[19] J. A. Hodge, K. V. Mishra, B. M. Sadler, and A. I. Zaghloul, "Performance analysis of spatial and frequency domain index-modulated reconfigurable intelligent metasurfaces," in *Proc. IEEE Int. Conf. Acoust., Speech, Signal Process.*, Toronto, Canada, Jun. 2021, pp. 8077–8081.

[20] T. Wei, L. Wu, K. V. Mishra, and M. B. Shankar, "Multiple IRS-assisted wideband dual-function radar-communication," in *Proc. Int. Symp. Joint Commun. Sens.*, Seefeld, Austria, Mar. 2022, pp. 1–5.

[21] Z. Zhang et al., "Active RIS vs. passive RIS: Which will prevail in 6G?," *IEEE Trans. Commun.*, vol. 71, no. 3, pp. 1707–1725, Mar. 2023.

[22] C. You and R. Zhang, "Wireless communication aided by intelligent reflecting surface: Active or passive?," *IEEE Wireless Commun. Lett.*, vol. 10, no. 12, pp. 2659–2663, Dec. 2021.

[23] Y. Pan, C. Pan, S. Jin, and J. Wang, "RIS-aided near-field localization and channel estimation for the terahertz system," *IEEE J. Sel. Topics Signal Process.*, vol. 17, no. 4, pp. 878–892, Jul. 2023.

[24] K. Zhi, C. Pan, H. Ren, K. K. Chai, and M. Elkashlan, "Active RIS versus passive RIS: Which is superior with the same power budget?," *IEEE Commun. Lett.*, vol. 26, no. 5, pp. 1150–1154, May 2022.

[25] A. M. Elbir, K. V. Mishra, and S. Chatzinotas, "NBA-OMP: Near-field beam-split-aware orthogonal matching pursuit for wideband THz channel estimation," in *Proc. IEEE Int. Conf. Acoust., Speech, Signal Process.*, Rhodes Island, Greece, 2023, pp. 1–5.

[26] A. M. Elbir, W. Shi, A. K. Papazafeiropoulos, P. Kourtessis, and S. Chatzinotas, "Near-field terahertz communications: Model-based and model-free channel estimation," *IEEE Access*, vol. 11, pp. 36409–36420, 2023.

[27] S. Palmucci, A. Guerra, A. Abrardo, and D. Dardari, "Two-timescale joint precoding design and RIS optimization for user tracking in near-field MIMO systems," *IEEE Trans. Signal Process.*, vol. 71, pp. 3067–3082, 2023.

[28] A. Elzanaty, A. Guerra, F. Guidi, D. Dardari, and M.-S. Alouini, "Toward 6G holographic localization: Enabling technologies and perspectives," *IEEE Internet Things Mag.*, vol. 6, no. 3, pp. 138–143, Sep. 2023.

[29] Z. Wang, Z. Liu, Y. Shen, A. Conti, and M. Z. Win, "Location awareness in beyond 5G networks via reconfigurable intelligent surfaces," *IEEE J. Sel. Areas Commun.*, vol. 40, no. 7, pp. 2011–2025, Jul. 2022.

[30] J. Zhang, Z. Zheng, Z. Fei, and Z. Han, "Energy-efficient multiuser localization in the RIS-assisted IoT networks," *IEEE Internet Things J.*, vol. 9, no. 20, pp. 20651–20665, Oct. 2022.

[31] M. S. Siraj, A. B. Rahman, M. Diamanti, E. E. Tsiropoulou, and S. Papavassiliou, "Alternative positioning, navigation, and timing enabled by games in satisfaction form and reconfigurable intelligent surfaces," *IEEE Syst. J.*, vol. 17, no. 3, pp. 5035–5046, Sep. 2023.

[32] C. Pan et al., "Reconfigurable intelligent surfaces for 6G systems: Principles, applications, and research directions," *IEEE Commun. Mag.*, vol. 59, no. 6, pp. 14–20, Jun. 2021.

[33] J. He, H. Wymeersch, L. Kong, O. Silvén, and M. Juntti, "Large intelligent surface for positioning in millimeter wave MIMO systems," in *Proc. IEEE Semiannual Veh. Technol. Conf.*, Antwerp, Belgium, May 2020, pp. 1–5.

[34] H. Zhang et al., "Metaradar: Indoor localization by reconfigurable metamaterials," *IEEE Trans. Mobile Comput.*, vol. 21, no. 8, pp. 2895–2908, Aug. 2022.

[35] O. Rinchi, A. Elzanaty, and M.-S. Alouini, "Compressive near-field localization for multipath RIS-aided environments," *IEEE Commun. Lett.*, vol. 26, no. 6, pp. 1268–1272, Jun. 2022.

[36] H. Wymeersch and B. Denis, "Beyond 5G wireless localization with reconfigurable intelligent surfaces," in *Proc. IEEE Int. Conf. Commun.*, Dublin, Ireland, Jun. 2020, pp. 1–6.

[37] T. Ma, Y. Xiao, X. Lei, W. Xiong, and Y. Ding, "Indoor localization with reconfigurable intelligent surface," *IEEE Commun. Lett.*, vol. 25, no. 1, pp. 161–165, Jan. 2021.

[38] Z. Zhang and L. Dai, "A joint precoding framework for wideband reconfigurable intelligent surface-aided cell-free network," *IEEE Trans. Signal Process.*, vol. 69, pp. 4085–4101, 2021.

[39] D. Dardari, N. Decarli, A. Guerra, and F. Guidi, "LOS/NLOS near-field localization with a large reconfigurable intelligent surface," *IEEE Trans. Wireless Commun.*, vol. 21, no. 6, pp. 4282–4294, Jun. 2022.

[40] M. He, W. Xu, H. Shen, G. Xie, C. Zhao, and M. D. Renzo, "Cooperative multi-RIS communications for wideband mmWave MISO-OFDM systems," *IEEE Wireless Commun. Lett.*, vol. 10, no. 11, pp. 2360–2364, Nov. 2021.

[41] S. Shrestha, A. C. Overvig, M. Lu, A. Stein, and N. Yu, "Broadband achromatic dielectric metalenses," *Light: Sci. Appl.*, vol. 7, no. 1, Nov. 2018, Art. no. 85.

[42] A. Y. Zhu et al., "Compact aberration-corrected spectrometers in the visible using dispersion-tailored metasurfaces," *Adv. Opt. Mater.*, vol. 7, no. 14, Jul. 2019, Art. no. 1801144.

[43] X. Qian and M. D. Renzo, "Mutual coupling and unit cell aware optimization for reconfigurable intelligent surfaces," *IEEE Wireless Commun. Lett.*, vol. 10, no. 6, pp. 1183–1187, Jun. 2021.

[44] S. Sun, Q. He, S. Xiao, Q. Xu, X. Li, and L. Zhou, "Gradient-index metasurfaces as a bridge linking propagating waves and surface waves," *Nature Mater.*, vol. 11, no. 5, pp. 426–431, May 2012.

[45] X. Xie et al., "Generalized pancharatnam-berry phase in rotationally symmetric meta-atoms," *Phys. Rev. Lett.*, vol. 126, no. 18, May 2021, Art. no. 183902.

[46] M. Z. Win, Y. Shen, and W. Dai, "A theoretical foundation of network localization and navigation," *Proc. IEEE*, vol. 106, no. 7, pp. 1136–1165, Jul. 2018.

[47] *Industrial Mobile Robots–Safety Requirements – Part 1: Requirements for the Industrial Mobile Robot*, American National Standards Institute/Robotic Industries Association Standard, ANSI/RIA R15.08-1-2020, 2020.

[48] W. Chung et al., "Safe navigation of a mobile robot considering visibility of environment," *IEEE Trans. Ind. Electron.*, vol. 56, no. 10, pp. 3941–3950, Oct. 2009.

[49] C. Yin, Z. Xiao, X. Cao, X. Xi, P. Yang, and D. Wu, "Offline and online search: UAV multiobjective path planning under dynamic urban environment," *IEEE Internet Things J.*, vol. 5, no. 2, pp. 546–558, Apr. 2018.

[50] Y. Shen and M. Z. Win, "Fundamental limits of wideband localization– Part I: A general framework," *IEEE Trans. Inf. Theory*, vol. 56, no. 10, pp. 4956–4980, Oct. 2010.

[51] Z. Wang, Z. Liu, Y. Shen, A. Conti, and M. Z. Win, "Wideband localization with reconfigurable intelligent surfaces," in *Proc. IEEE Semiannual Veh. Technol. Conf.*, Helsinki, Finland, Jun. 2022, pp. 1–6.

[52] L. Dai et al., "Reconfigurable intelligent surface-based wireless communications: Antenna design, prototyping, and experimental results," *IEEE Access*, vol. 8, pp. 45913–45923, 2020.

[53] J. C. Liang et al., "An angle-insensitive 3-bit reconfigurable intelligent surface," *IEEE Trans. Antennas Propag.*, vol. 70, no. 10, pp. 8798–8808, Oct. 2022.

[54] C. A. Balanis, *Antenna Theory: Analysis and Design*. Hoboken, NJ, USA: Wiley, 2016.

[55] S. Zhang and R. Zhang, "Capacity characterization for intelligent reflecting surface aided MIMO communication," *IEEE J. Sel. Areas Commun.*, vol. 38, no. 8, pp. 1823–1838, Aug. 2020.

Ziyi Wang (Graduate Student Member, IEEE) received the B.E. (with highest honor) in School of Electronic and Information Engineering from Beihang University in 2020. He is working toward the M.S. degree at ETH Zurich, Switzerland.

He was with the Wireless Information and Network Sciences Laboratory, Massachusetts Institute of Technology (MIT) from 2020 to 2022. His research interests include wireless communication, network localization, and reconfigurable intelligent surfaces. He received national scholarships from 2016 to 2018. He served as a reviewer of various IEEE journals and international conferences.

Zhenyu Liu (Member, IEEE) received the Ph.D. degree in networks and statistics from the Massachusetts Institute of Technology (MIT) in 2022. He received the B.S. degree (with honor) and M.S. degree in electronic engineering from Tsinghua University, Beijing, China, in 2011 and 2014, respectively.

Currently, he is an Assistant Professor at Tsinghua Shenzhen International Graduate School, Tsinghua University, China. His research interests include wireless communications, network localization, distributed inference and learning, networked control, and quantum information science.

Dr. Liu received the first prize of the IEEE Communications Society's Student Competition in 2016 and 2019, a Research and Development 100 Award for Peregrine System in 2018, and the Best Paper Award at the IEEE Latin-American Conference on Communications in 2017.

Yuan Shen (Senior Member, IEEE) received the B.E. degree in electronic engineering from Tsinghua University in 2005, and the S.M. degree and the Ph.D. degree in electrical engineering and computer science from the Massachusetts Institute of Technology (MIT) in 2008 and 2014, respectively.

He is currently a Full Professor with the Department of Electronic Engineering at Tsinghua University. His research interests include network localization and navigation, integrated sensing and control, and multi-agent systems. His papers have received the IEEE ComSoc Fred W. Ellersick Prize and several best paper awards from IEEE conferences. He has served as the TPC Symposium CoChair for IEEE ICC and IEEE Globecom for several times. He was the Elected Chair for the IEEE ComSoc Radio Communications Committee from 2019 to 2020. He is an Editor of the IEEE Transactions on Signal Processing, IEEE Transactions on Communications, IEEE Transactions on Network Science and Engineering, and *China Communications*.

Andrea Conti (Fellow, IEEE) is a Professor and founding director of the Wireless Communication and Localization Networks Laboratory at the University of Ferrara, Italy. Prior to joining the University of Ferrara, he was with CNIT and with IEIITCNR.

In Summer 2001, he was with the Wireless Systems Research Department at AT&T Research Laboratories. Since 2003, he has been a frequent visitor with the Wireless Information and Network Sciences Laboratory at the Massachusetts Institute of Technology, where he presently holds the Research Affiliate appointment. His research interests involve the theory and experimentation of wireless communication and localization systems. His current research topics include network localization and navigation, distributed sensing, adaptive diversity communications, and quantum information science.

Dr. Conti has served as editor for IEEE journals and chaired international conferences. He was elected Chair of the IEEE Communications Society's Radio Communications Technical Committee and is Co-founder of the IEEE Quantum Communications and Information Technology Emerging Technical Subcommittee. He received the HTE Puskás Tivadar Medal, the IEEE Communications Society's Fred W. Ellersick Prize, and the IEEE Communications Society's Stephen O. Rice Prize in the field of Communications Theory. He is an elected Fellow of the IET and a member of Sigma Xi. He has been selected as an IEEE Distinguished Lecturer.

Moe Z. Win (Fellow, IEEE) is the Robert R. Taylor Professor at the Massachusetts Institute of Technology (MIT) and the founding director of the Wireless Information and Network Sciences Laboratory. Prior to joining MIT, he was with AT&T Research Laboratories and with the NASA Jet Propulsion Laboratory.

His research encompasses fundamental theories, algorithm design, and network experimentation for a broad range of real-world problems. His current research topics include ultra-wideband systems, network localization and navigation, network interference exploitation, and quantum information science. He has served the IEEE Communications Society as an elected Member-at-Large on the Board of Governors, as elected Chair of the Radio Communications Committee, and as an IEEE Distinguished Lecturer. Over the last two decades, he held various editorial positions for IEEE journals and organized numerous international conferences. He has served on the SIAM Diversity Advisory Committee.

Dr. Win is an elected Fellow of the AAAS, the EURASIP, the IEEE, and the IET. He was honored with two IEEE Technical Field Awards: the IEEE Kiyo Tomiyasu Award (2011) and the IEEE Eric E. Sumner Award (2006, jointly with R. A. Scholtz). His publications, coauthored with students and colleagues, have received several awards. Other recognitions include the MIT Frank E. Perkins Award (2024), the MIT Everett Moore Baker Award (2022), the IEEE Vehicular Technology Society James Evans Avant Garde Award (2022), the IEEE Communications Society Edwin H. Armstrong Achievement Award (2016), the Cristoforo Colombo International Prize for Communications (2013), the Copernicus Fellowship (2011) and the *Laurea Honoris Causa* (2008) from the Università degli Studi di Ferrara, and the U.S. Presidential Early Career Award for Scientists and Engineers (2004).